Featured in Physics

More is Less in Unpercolated Active Solids

Jack Binysh[1,*] Guido Baardink[2] Jonas Veenstra[1] Corentin Coulais[1,†] and Anton Souslov[3,‡]

[1]Institute of Physics, Universiteit van Amsterdam, 1098 XH Amsterdam, The Netherlands
[2]Department of Physics, University of Bath, Claverton Down, Bath BA2 7AY, United Kingdom
[3]TCM Group, Cavendish Laboratory, JJ Thomson Avenue, Cambridge, CB3 0US, United Kingdom

(Received 25 April 2025; accepted 5 February 2026; published 13 April 2026)

A remarkable feat of active matter physics is that systems as diverse as collections of self-propelled particles, nematics mixed with molecular motors, and interacting robots can all be described by symmetry-based continuum theories. These descriptions rely on reducing complex effects of individual motors to a few key active parameters, which increase with activity. Here we observe a striking anomaly in the continuum description of nonreciprocal active solids, a ubiquitous class of active materials. Using a combination of metamaterial experiments and coarse-graining theory we find that as microscopic activity increases, macroscale active response can vanish: more is less. In this highly active regime, nonaffine and localized modes prevail and destroy the large-scale signature of microscopic activity. These modes exist in any dilute periodic structure and emerge in random lattices below a percolation transition. Our results unveil a counterintuitive facet of active matter, offering new principles for engineering materials far from equilibrium.

DOI: 10.1103/flhb-kjyd

Subject Areas: Metamaterials, Soft Matter

The stiffer the steel—the stiffer the bridge. This principle broadly applies to mechanical structures in equilibrium: By rigidifying even a single component, the entire structure becomes more rigid. Beyond architecture, this idea connects structure with function in any material, from polymers and glasses to nano- and metamaterials. This one-to-one connection derives from the same logic that guarantees stability in mechanical equilibrium, and is more generally known as Le Chatelier's principle. The principle dictates that near equilibrium, a system will counteract an external stimulus. Related concepts also apply to fluidic, electric, and chemical networks, and form the foundation of materials mechanics.

Active materials—composed of units that use ambient energy to exert local forces, pushing the system far from equilibrium [1,2]—routinely challenge the principles of thermodynamics. These materials unlock properties that are traditionally forbidden, from long-range orientational order in two dimensions and phase separation in the absence of attraction [3] to time-crystalline states [4–7]. Active solids [8–14] combine this far-from-equilibrium character with a stable reference state, in sharp contrast to the instabilities and nonlinearities that plague many active systems [15]. Significantly, even away from the stable state, these materials exhibit well-controlled dynamics [16], which can be tuned via external stimuli [17,18]. These features make active solids especially attractive for functional materials, but being far from equilibrium presents a challenge in designing their linear response. Here we ask a basic question: when does Le Chatelier's principle, including the monotonicity of macroscale rigidity with microscale stiffness, break down in active solids?

To address this question, we focus on nonreciprocal active matter, which is found in contexts as diverse as spins [19–21], optomechanical devices [22–25], optics [26], acoustics [27,28], hydrodynamics [29–31], reaction-diffusion chemistry, and colloidal physics [32–37]. Crucially, nonreciprocity can also be defined at the level of mechanics [38,39], where the nonequilibrium nature of linear response manifests itself via amplified waves and linear work cycles. However, in all of those studies, Le Chatelier's principle is respected: the macroscopic response is monotonic in the microscopic activity.

Here we create materials in which increasing the microscopic activity weakens linear response, violating Le Chatelier's principle. Combining experiments on robotic metamaterials with analytical coarse graining, we discover that this anomalous behavior is rooted in a percolation transition within the active parts of the elastic solid. Below percolation, active floppy modes emerge, which kill the

*Contact author: j.a.c.binysh@uva.nl
†Contact author: coulais@uva.nl
‡Contact author: as3546@cam.ac.uk

Published by the American Physical Society under the terms of the Creative Commons Attribution 4.0 International license. Further distribution of this work must maintain attribution to the author(s) and the published article's title, journal citation, and DOI.

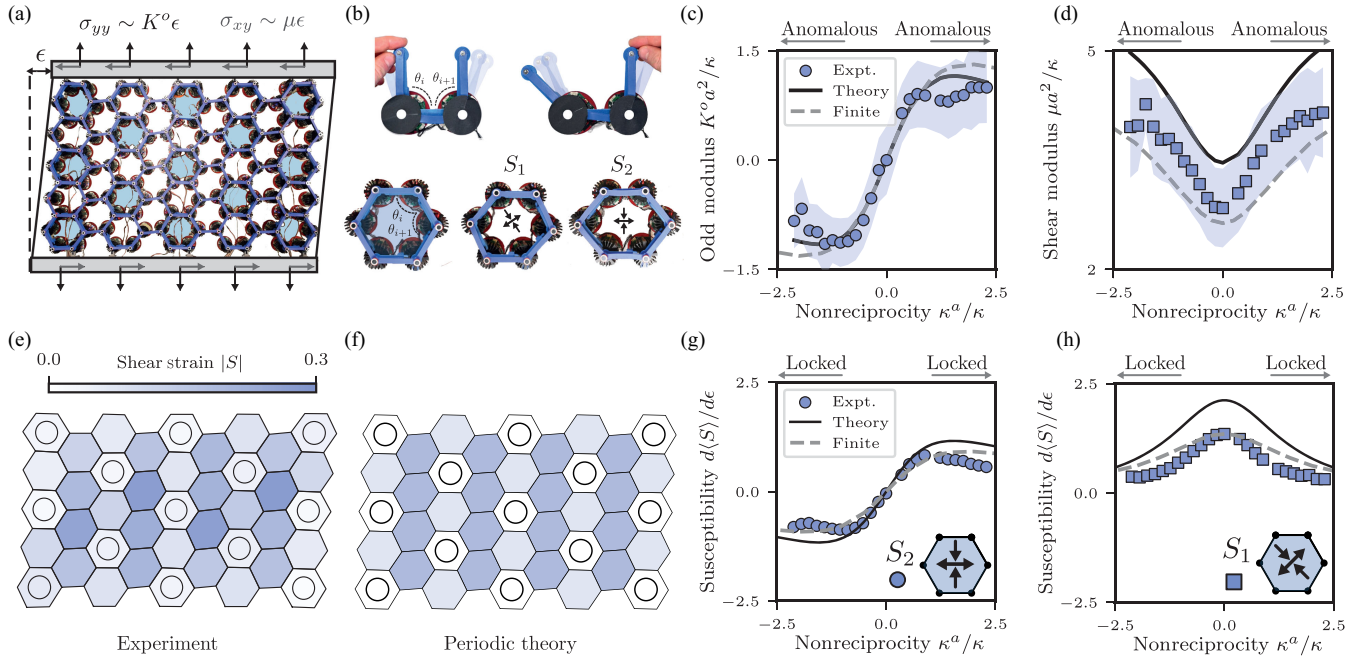


FIG. 1. Anomalous odd response in nonreciprocal materials. Transversely shearing an isotropic lattice built from nonreciprocal plaquettes generates normal stresses, the hallmark of odd elasticity. These odd moduli break equilibrium conditions of monotonic response, and can anomalously vanish as microscopic activity increases. (a)–(b) A robotic metamaterial built from a mixture of active (blue highlights) and passive hexagonal plaquettes. Each active plaquette is made from three bar linkages (side length a). Motors on each linkage vertex exert torques according to a nonreciprocal torque-angle relation $\tau_i = \kappa^a(\delta\theta_{i+1} - \delta\theta_{i-1})$, alongside a passive elastic response $\tau_i = -\kappa\delta\theta_i$. The lowest deformation modes of these plaquettes are the transverse S_1 and vertical S_2 shears. (c),(d) Shearing the lattice reveals an anomalous regime where the odd modulus K^o decreases as microscale nonreciprocity κ^a diverges, with crossover occurring at $\kappa^a/\kappa \sim 1$. Concomitantly, the shear modulus μ actively stiffens. Points correspond to experimental runs, with error bars quantifying the spread of force sensor measurements on either side of the metamaterial. Solid curves indicates coarse-grained periodic theory. Dashed gray curves indicate ball-spring simulations that account for finite-size effects. (e),(f) Visualizing the strain field within the lattice in experiment and periodic theory reveals a nonaffine checkerboard pattern in which active plaquettes lock, admitting no shear deformation at all. Plaquette colors show hexagonal strain $|S| = \sqrt{S_1^2 + S_2^2}$, with active plaquettes indicated by inset circles. (g),(h) To track the plaquette-level response to an applied shear ϵ, we average the strain over all active plaquettes, $\langle S\rangle$, and then compute the susceptibility $d\langle S\rangle/d\epsilon$ as a function of activity κ^a. We find that the anomalous plaquette-locked regime emerges at high activity, with crossover in the shear modes occurring concurrently with the peak and decay of the odd modulus.

macroscopic manifestation of microscale activity. At the same time that continuum response fails to capture the signatures of nonreciprocity, we discover a proliferation of active higher-frequency optical modes. Our work establishes the percolation of active units as a general principle for understanding active solids, with applications ranging from the design of self-learning networks [40–43] and mechanical metamaterials [17,18,44] to the dynamics of biological lattices [13,14,45–47].

We first illustrate how macroscale nonreciprocal response can vanish even as microscale nonreciprocity increases. Figure 1(a) shows a robotic metamaterial built from hexagonal plaquettes of torque motors. When the motors are off, each hinge in the lattice has a passive torque-angle relation $\tau_i = -\kappa\delta\theta_i$ with stiffness κ. Within each active plaquette [Fig. 1(a), blue highlights] the ith motor additionally exerts an active torque $\tau_i = \kappa^a(\delta\theta_{i+1} - \delta\theta_{i-1})$ via an antisymmetric combination of neighboring angular deflections $\delta\theta_{i+1}, \delta\theta_{i-1}$ [Fig. 1(b)] (Appendix IX and Supplemental Material movie S1 [48]). This microscale antisymmetry, quantified by κ^a, breaks Maxwell-Betti reciprocity and generates an antisymmetric coupling between the horizontal S_1 and vertical S_2 shear modes of the lattice.

We apply a macroscopic transverse strain $\epsilon \sim S_1$ to the lattice and measure both normal and tangential shear stresses, σ_{yy} and σ_{xy} [Fig. 1(a)]—in Appendix X and Fig. 12 we detail our experimental protocol and show full stress-strain sweeps. Large-scale nonreciprocal response is quantified by the odd modulus, $K^o = d\sigma_{yy}/d\epsilon$ at $\epsilon = 0$. This linear modulus vanishes for passive materials. Previous measurements of odd elasticity have been inferred indirectly from displacement data [16] in highly dynamic, fluctuating active solids [9,30], which can be complicated by noise [49] or additional degrees of freedom [47]. Here our robotic platform and experimental setup allow a direct measurement of K^o from stress-strain data in the static regime.

For weak nonreciprocity κ^a, we measure a monotonic response, $K^o \sim \kappa^a$. Yet on further increase of κ^a we observe a peak and subsequent decay of K^o [Fig. 1(c)], accompanied by an active stiffening of the linear shear modulus $\mu = d\sigma_{xy}/d\epsilon$ [Fig. 1(d)]. The anomalous response in K^o vs κ^a stands in stark contrast to the scaling of elastic moduli with the stiffness of microscopic building blocks in passive isotropic materials, which must be monotonic (Appendix IV).

To unravel the cause of the anomalous decay of K^o and active stiffening of μ, we develop and coarse-grain a periodic model of our metamaterial to analytically predict its elastic moduli. In Secs. II–III in the Appendix we give compact expressions for the moduli and internal deformations of a generic nonreciprocal lattice built from nonpairwise interactions, such as those shown in Fig. 1. Our theory predicts that

$$K^o = \frac{3}{2}\frac{\kappa^a}{a^2}\frac{1}{1+c_1(\kappa^a/\kappa)^2},$$
$$\mu = 2\sqrt{3}\frac{\kappa}{a^2}\frac{1+c_2(\kappa^a/\kappa)^2}{1+c_1(\kappa^a/\kappa)^2}, \quad (1)$$

where a is the hexagonal side length of a single linkage, and $c_2 = 45/64 > c_1 = 27/64$ are positive numerical constants that reflect the geometry of the lattice. We predict that K^o peaks when $\kappa^a/\kappa \sim 1$, before decaying as $K^o \sim \kappa^2/\kappa^a$ in the limit of large activity. In this same limit, we also predict that the shear modulus μ plateaus at $\mu = 2\sqrt{3}\kappa c_2/c_1$, a rescaled value above the passive $\kappa^a = 0$ limit. This peak in K^o and active stiffening of μ are both in good agreement with our experiments [Figs. 1(c) and 1(d)].

Our periodic theory has a systematic overshoot relative to experiment, particularly in the shear modulus μ [Fig. 1(d)]. By developing ball-spring simulations of our metamaterials, we find that the dominant cause of this discrepancy is finite-size effects, which are caused by the relatively small number of unit cells in our experiment (Appendix VIII, Figs. 10 and 11). However, the twin signatures that our theory predicts—a peak in K^o and a stiffening μ—are robust to these experimental imperfections. What is the mechanism behind these phenomena?

We characterize the micromechanics underpinning these effects by projecting the deformations of every plaquette onto the shear modes of a single hexagon [Figs. 1(e) and 1(f)]. At large activity we observe a highly nonaffine checkerboard of deformations: In both experiment and periodic theory the magnitude of the strain $\langle|S|\rangle = \langle\sqrt{S_1^2+S_2^2}\rangle$ in the active plaquettes vanishes [Figs. 1(e) and 1(f)]. To better quantify this observation, we first fix κ^a, and measure sweeps of applied strain ϵ against plaquette-level shear S (Fig. 12). The slopes of these relations, $dS/d\epsilon$ for S_1 and S_2, measure how susceptible a given hexagon is to the externally applied strain, and into which mode it will shear.

We now vary κ^a and track the susceptibilities $d\langle S\rangle/d\epsilon$ averaged across active plaquettes [Figs. 1(g) and 1(h)]. When $\kappa^a = 0$ all hexagons are passive and the shear in each plaquette follows the applied strain field: $S_1 \sim \epsilon$ dominates with $S_2 \approx 0$. As κ^a increases, $d\langle S_2\rangle/d\epsilon$ peaks as the coupling between shear modes generates a normal shear strain $S_2 \sim K^o S_1$. However, as activity further increases S_2 and S_1 both decay: the active plaquettes lock, and the passive degrees of freedom shoulder the entire strain field applied to the sample boundary. Our systematic sweep of $d\langle S\rangle/d\epsilon$ against κ^a [Figs. 1(g) and 1(h)] demonstrates that the locking behavior underpinning the checkerboard in Figs. 1(e) and 1(f) emerges only at high activity.

The link between micro- and macroscale nonreciprocity is therefore subtle: Figure 1 shows a structure which is highly nonreciprocal yet possesses decaying odd response, in contrast to the monotonic structure-function link exhibited by recent examples of living and synthetic active solids [9,16,47]. To uncover the structural motifs that separate monotonic and nonmonotonic materials, we use our analytic coarse-graining procedure to numerically generate a family of honeycomb lattices containing a varying fraction p of active plaquettes, and calculate their theoretical elastic moduli and internal strains under compression (Fig. 2 and Supplemental Material movie S2 [48]). We vary p either through periodic dilutions of a fully tiled lattice [Figs. 2(a)–2(d)] or via random removals of active plaquettes [Figs. 2(e)–2(h)]—in Appendix VI we detail our analytical results for periodic lattices, and numerical procedure for calculating the moduli of random structures.

For $p \approx 1$ [Figs. 2(a), 2(b), 2(e), and 2(f)], our numerics show that active plaquettes strain in system-spanning clusters, with a corresponding nonzero odd response [Figs. 2(i) and 2(k)]. However, at $p = p_c = 1/2$, we cross the site percolation threshold for the triangular Bravais lattice on which the hexagonal plaquettes sit. Below the percolation threshold active plaquettes decouple from one another [Figs. 2(c), 2(d), 2(g), and 2(h)]: Each plaquette independently rigidifies, and odd response is lost [Figs. 2(i) and 2(k)]. Just beneath p_c [Figs. 2(b), 2(c), 2(f), and 2(g)], these suddenly rigid plaquettes occupy a substantial fraction of the sample, causing a spike in the passive shear modulus μ [Figs. 2(j) and 2(j)] which coincides with the jump in the active modulus K^o [Figs. 2(i) and 2(k)]. This spike in μ then decays as p tends to zero [Fig. 2(k)] and rigid units are further removed from the lattice. These twin behaviors—a jump in K^o and a spike in μ—are not restricted to on-lattice disorder, but also occur even in positionally disordered structures (Appendix VII). In summary, the lattice connectivity itself mediates a transition into an anomalous nonmonotonic regime in K^o as a function of κ^a, alongside an active stiffening of the passive modulus μ.

Motivated by the crucial role of p in the onset of anomolous odd response, we compare the force balance in two lattices that lie on either side of percolation (Fig. 3).

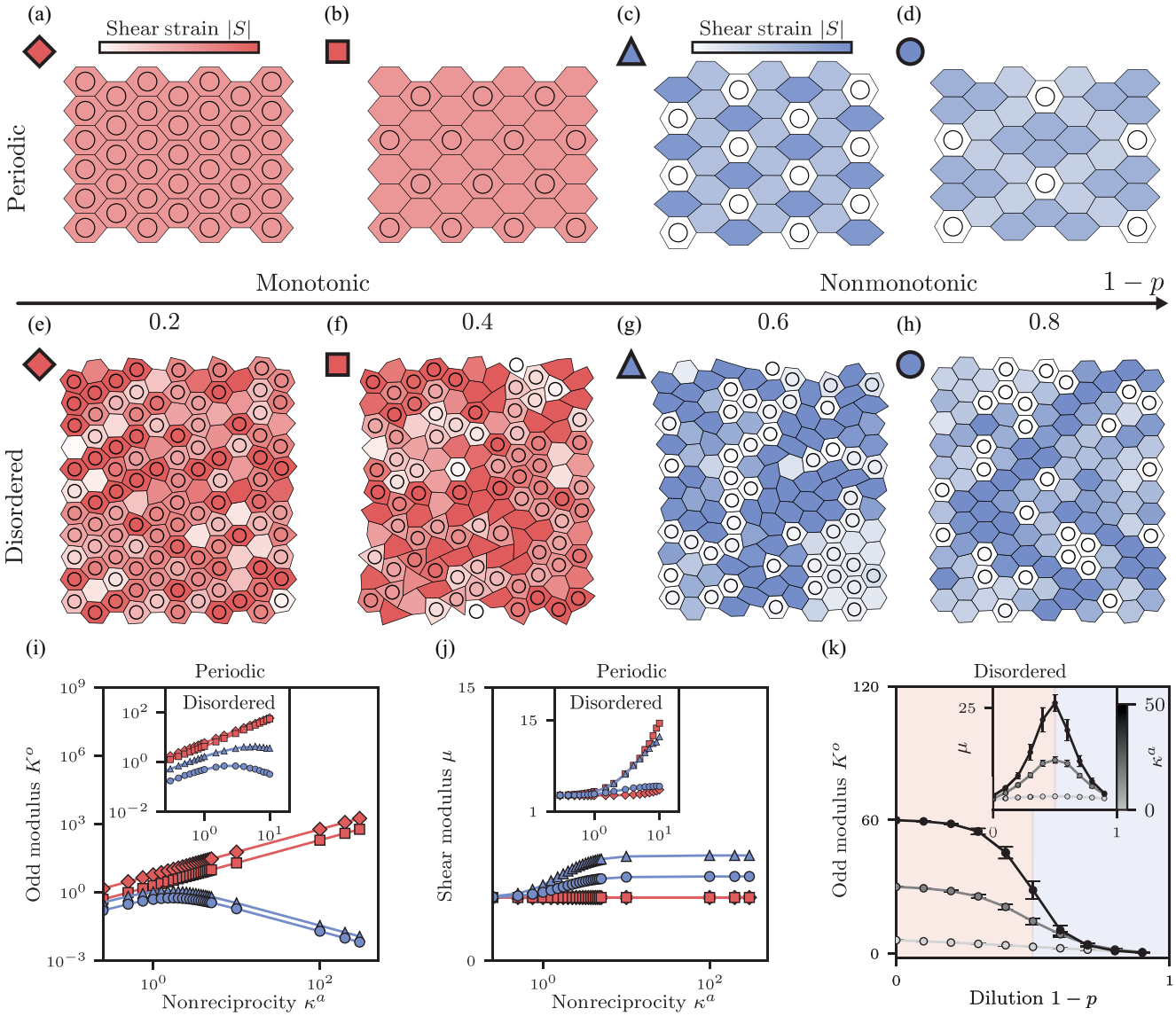


FIG. 2. Odd response vanishes via a percolation transition in active degrees of freedom. (a)–(h) We remove active plaquettes from ball-spring models of a fully tiled honeycomb lattice, either through isotropy-preserving periodic dilutions (a)–(d) or through random removals with probability $1-p$ (e)–(h). For large p, active plaquettes deform in system-spanning clusters, generating odd response. For small p, these plaquettes decouple from one another, and the strain in the active units vanishes. Colors show strain magnitude $|S|$ per plaquette under a vertical pure shear strain $\epsilon = 0.05$. Red and blue dichotomy indicates lattices with monotonic and nonmonotonic odd response at large activity. Panels (e)–(h) show typical random realizations at $1-p = 0.2, 0.4, 0.6, 0.8$. (i),(j) Dilutions either exhibit monotonic or anomalous $K^o(\kappa^a)$, with accompanying active stiffening of $\mu(\kappa^a)$, as the active plaquette fraction p decreases and active force chains are destroyed. Markers in main panels show results for the structured lattices in (a)–(d). Markers in insets correspond to averages over random lattices (e)–(h). (k) Varying p continuously in random lattices (e)–(h), we find a step jump in $K^o(p)$ and a spike in $\mu(p)$ as p crosses the percolation threshold $p = p_c = 1/2$. Error bars denote standard deviations of the fluctuating quantities K^o and μ. Throughout the figure $\kappa = a = 1$.

We first boil the complexity of our honeycomb lattices down to a minimal model: a triangular lattice composed of longitudinal springs with finite stiffness k, where each triangular plaquette also hosts nonreciprocal longitudinal springs [Fig. 3(a)]. These springs exert tensions $k^a(\delta L_{i+1} - \delta L_{i-1})$ in response to length changes δL of neighboring bonds. Straining a single plaquette of these nonreciprocal springs generates an antisymmetric bond tension field which is skewed at an angle to the applied load [Fig. 3(b)]. We now attempt to tile this skewed tension field across a lattice, in order to build system-spanning tension chains that generate odd elastic response.

We first consider a half tiled lattice [Fig. 3(c)], for which we predict a monotonic odd response $K^o = 3k^a/4$.

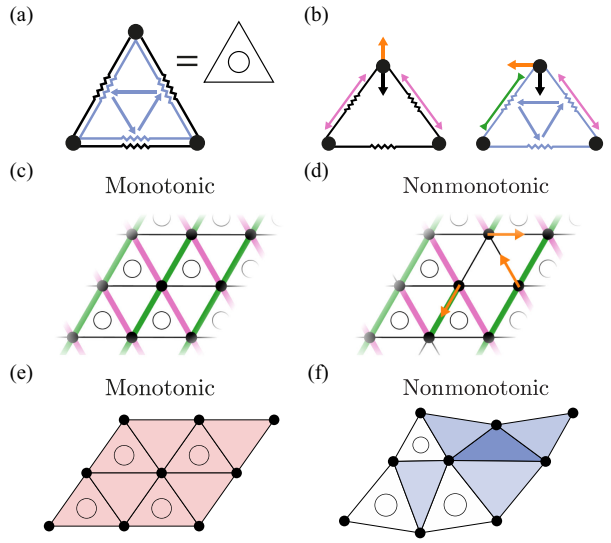


FIG. 3. The anatomy of vanishing odd response. (a) A minimal model for vanishing odd response and plaquette locking: A triangular plaquette made of extensional springs with stiffness k (black), and nonreciprocal springs (blue) with tension law $T_i = k^a(\delta L_{i+1} - \delta L_{i-1})$. Blue directed arrows show the neighbors of a given bond. (b) Compressing passive springs generates a symmetric tension field (pink) and restoring force (orange) parallel to the applied load (black). Compressing nonreciprocal springs generates a tension field (green, pink arrows) and restoring force which are skewed. (c),(d) System-spanning active force chains are only possible in certain lattice geometries. Panel (c) shows a successful chain in a $p = 1/2$ activated lattice. In the $p = 3/8$ activated lattice (d) we cannot construct a chain. When active plaquettes are sheared, we necessarily find unbalanced nodal forces. This lattice cannot support odd response at high activity. (e),(f) Force-balanced displacement fields under vertical applied shear for $k^a \gg k$, colored by shear strain magnitude. In the underpercolated $p = 3/8$ lattice, active plaquettes do not shear.

Examining the tension chains in this lattice under shear, we find that our plaquette-level tensions can be successfully tiled across the entire sample. We now attempt the same tiling process for an underpercolated lattice with $p = 3/8$, for which our theory predicts $K^o \sim k^2/(k^a)$ at large k^a (Appendix VI) [Fig. 3(d)]. We discover a crucial feature in the tension field within this dilute lattice: we inevitably encounter masses at which active forces cannot be balanced. At finite passive stiffness k, these unbalanced active forces are counteracted by passive elasticity. However, as $k^a/k \to \infty$ we have a separation of scales, and active forces must balance against one another. Therefore, instead of balancing active forces across unit cells, the $p = 3/8$ lattice balances them within individual plaquettes.

The consequence of this local active force balance is shown in Figs. 3(e) and 3(f), where we examine the equilibrium configurations of both triangular lattices under shear: our model exhibits the same locked states, and nonaffine checkerboards, as we observe in our experimentally constructed metamaterials [Figs. 1(d) and 1(e)] (Appendix V). Intuitively, nonreciprocal tensions are screened out at high activity. The resulting intercell tension field is then found by minimizing the energy of an effectively passive lattice, which must have $K^o = 0$. This reduced lattice also has fewer degrees-of-freedom than the original lattice, because of the additional constraints of active force balance. Adding these constraints rigidifies the lattice, increasing μ.

If the odd modulus of a nonreciprocal material vanishes, what are the remaining signatures of activity? In Fig. 4, we show that the vibrational spectrum of an underpercolated active lattice differs dramatically from passive materials, even in the limit of vanishing K^o. We consider again lattices of nonreciprocal triangular plaquettes, such as those shown in Fig. 3, and focus on the high activity limit $k^a/k \to \infty$. By diagonalizing the lattice dynamical matrix, we obtain the vibrational eigenspectrum ω (Appendix VI). Because the dynamical matrix is non-Hermitian, ω is in general complex: under an overdamped dynamics, $\mathrm{Re}(\omega)$ would correspond to relaxation and $\mathrm{Im}(\omega)$ to oscillations.

For large p, we find two branches of complex eigenmodes [Figs. 4(a) and 4(e)], inherited from the phonon structure of a fully tiled active lattice. These oscillatory phonons are the long-wavelength signature of microscopic nonreciprocity, with the slope of each branch in the complex plane quantifying the odd modulus, $\mathrm{Im}(\omega)/\mathrm{Re}(\omega) \sim K^o/\mu$ [50]. As active plaquettes are removed from the lattice, these phononic bands collapse to the $\mathrm{Re}(\omega)$ axis as K^o vanishes [Figs. 4(b), 4(c), 4(f), and 4(g)]. Indeed in Fig. 8 and Table I in the Appendix, we show that these triangular lattices show a decay of K^o with decreasing p, and a spike in μ at intermediate p, that is analogous to that shown in Figs. 2(i) and 2(j). Yet even as this collapse occurs, we find that a second branch of modes remains complex: The spectrum splits into two pieces, and an active phonon gap in $\mathrm{Re}(\omega)$ opens. Within the gap, the vibrations of the material appear effectively passive. Beyond the gap, oscillations emerge at complex frequencies. In Figs. 4(d) and 4(h) we quantify the appearance of this gap as a function of plaquette fraction p. We find that vanishing of the slope of the phononic bands and the emergence of the active phonon gap occur simultaneously, both coinciding with the $p = 1/2$ site percolation threshold for removal of triangular plaquettes.

What is the spatial structure of the lattice vibrations that underpin this active phonon gap? In Figs. 4(i)–4(k) we take a single underpercolated lattice and visualize the deformation fields which live in each branch of the eigenspectrum [Fig. 4(g)]. We find that complex modes with nonzero $\mathrm{Im}(\omega)$ are composed of highly nonaffine displacement fields localized around a single active plaquette: even in an overdamped scenario this plaquette would oscillate with substantial shear strain [Fig. 4(i)]. In stark contrast, we find that eigenmodes lying on the real axis exhibit no shear in the active plaquettes at all. Instead, the shear of the passive

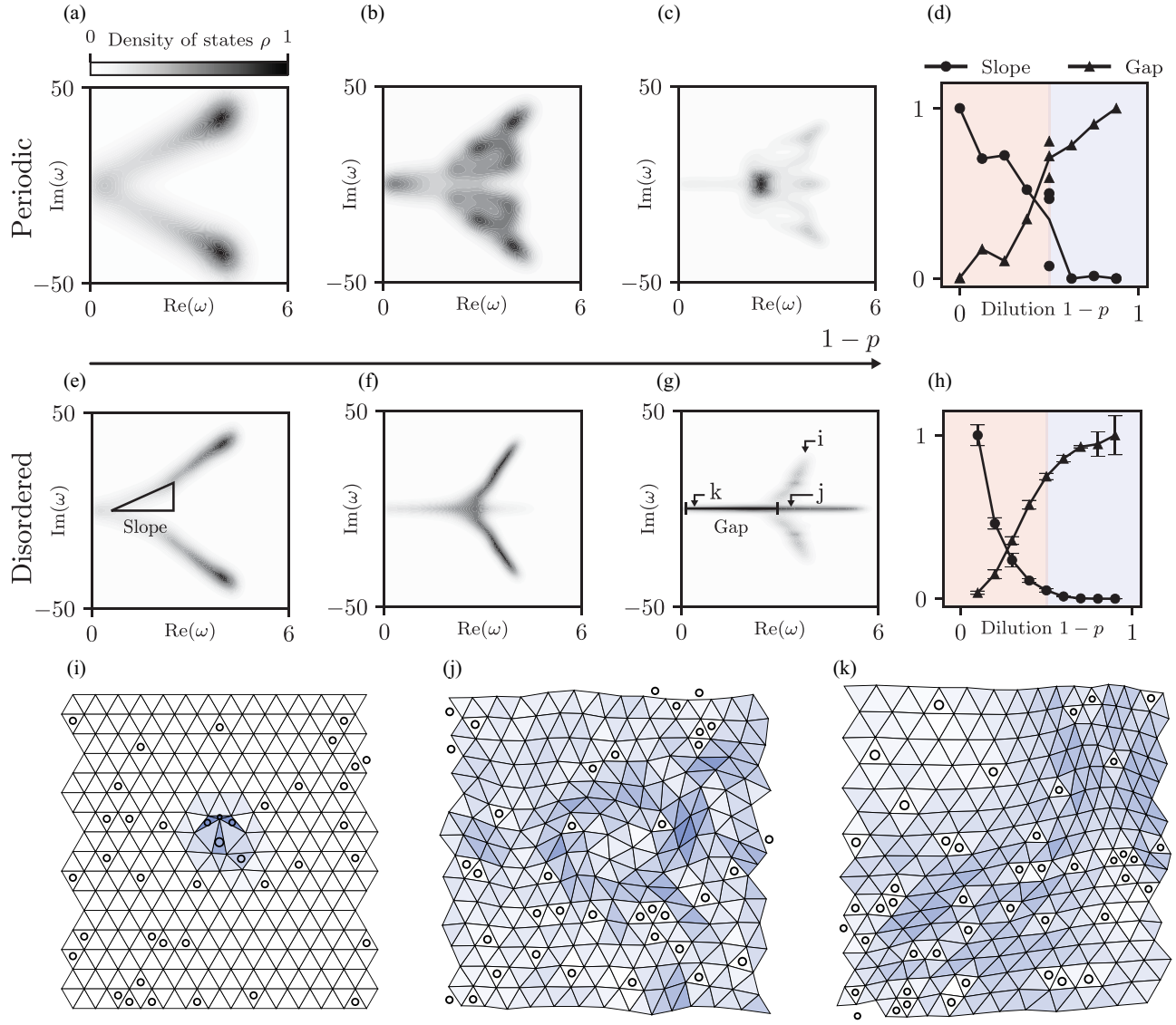


FIG. 4. Underpercolated lattices exhibit an active phonon gap in their vibrational spectrum. As active plaquettes are removed from ball-spring models of a fully tiled triangular lattice, the vibrational eigenspectrum ω splits into two discrete lobes—an effectively passive component with $\mathrm{Im}(\omega) = 0$ which contains lattice phonons, and highly localized vibrations at complex ω. The eigenvalues ω are expressed in units of the spring stiffness k. (a)–(c) The density of states $\rho(\omega)$ for three periodic dilutions of a fully tiled active triangular lattice at $k^a/k = 5$ [(a) $p = 1$, (b) $p = 5/8$, (c) $p = 3/8$]. For $p \approx 1$ we find phonon bands continuously connected to the origin, whose slope in the complex plane quantifies K^o. Yet as p is decreased, these bands collapse to the $\mathrm{Re}(\omega)$ axis, leaving lobes of active modes at complex ω gapped from the origin. Eigenvalues ω are given in units where $k = 1$. (e)–(g) Random dilutions [(e), $p = 0.9$, (f) $p = 0.5$, (g) $p = 0.2$] exhibit the same spectral collapse as their structured counterparts. (d),(h) A bilinear fit of $\rho(\omega)$ quantifies both the slope at the origin and active phonon gap. We find that K^o vanishes as the gap opens and p crosses $p_c = 1/2$. In panel (d), data points correspond to all isotropic dilutions of a 2×4 supercell of active plaquettes (Appendix VI). Three periodic lattices exist at $p = 1/2$, with interlattice variations in these metrics—we show data for each lattice, with the line denoting an average. In panel (h), the error bars quantify fluctuations in fits between samples. For ease of comparison, we normalize both slope and gap data by their largest value to lie in [0, 1]. (i)–(k) The eigenstates of a dilute lattice [panel (g)] reveal that modes at complex ω are composed of highly localized oscillations of individual plaquettes (i), whereas modes living on the $\mathrm{Re}(\omega)$ axis exhibit the swirls (j) and quasiplane waves (k) of an effectively passive spring network, interspersed with unsheared active plaquettes that act as a source of disorder. Color shows the shear strain in each plaquette under the corresponding normalized eigenvector displacement field.

units alone exhibits the midfrequency swirls [Fig. 4(j)] and low-frequency quasiplane waves [Fig. 4(k)] which are characteristic of a passive granular material or disordered spring network [51]. When active plaquettes are too dilute to couple with one another, activity no longer enables the collective motion and wave propagation captured in a continuum description, but instead powers highly localized oscillations.

TABLE I. Odd K^o and shear μ moduli for the ten linearly isotropic dilutions of the tile consisting of eight extension-active triangles, classified according to the asymptotic behavior of K^o at large k^a, which is also shown.

Lattice	p	Odd modulus K^o	Shear modulus μ	Classification
	8/8	$\frac{3k^a}{2}$	$\frac{\sqrt{3}}{4}$	Monotonic
	7/8	$\frac{3(14k^4k^a+79k^2k^{a3}+80k^{a5})}{8(4k^4+23k^2k^{a2}+25k^{a4})} \to k^a$	$\frac{\sqrt{3}(8k^5+49k^3k^{a2}+62kk^{a4})}{8(4k^4+23k^2k^{a2}+25k^{a4})}$	Monotonic
	6/8	$\frac{9k^a}{8}$	$\frac{\sqrt{3}}{4}$	Monotonic
	5/8	$\frac{3(20k^4k^a+79k^2k^{a3}+56k^{a5})}{4(16k^4+68k^2k^{a2}+49k^{a4})} \to k^a$	$\frac{\sqrt{3}(16k^5+74k^3k^{a2}+55kk^{a4})}{4(16k^4+68k^2k^{a2}+49k^{a4})}$	Monotonic
	4/8	$\frac{3k^a}{4}$	$\frac{\sqrt{3}}{4}$	Monotonic
	4/8	$\frac{3k^a}{4}$	$\frac{\sqrt{3}}{4}$	Monotonic
	4/8	$\frac{3(4k^2k^a+k^{a3})}{16(k^2+k^{a2})} \to k^a$	$\frac{\sqrt{3}(2k^3+5kk^{a2})}{8(k^2+k^{a2})}$	Monotonic
	3/8	$\frac{9(4k^4k^a+5k^2k^{a3})}{4(16k^4+20k^2k^{a2}+k^{a4})} \to \frac{1}{k^a}$	$\frac{\sqrt{3}(16k^5+26k^3k^{a2}+7kk^{a4})}{4(16k^4+20k^2k^{a2}+k^{a4})}$	Nonmonotonic
	2/8	$\frac{3k^a}{8}$	$\frac{\sqrt{3}}{4}$	Monotonic
	1/8	$\frac{3k^2k^a}{16k^2+12k^{a2}} \to \frac{1}{k^a}$	$\frac{\sqrt{3}k(8k^2+9k^{a2})}{8(4k^2+3k^{a2})}$	Nonmonotonic

In this work, we have explored nonreciprocity across scales in active solids, and discovered a regime where more is less: increasing activity on the microscale can decrease it at the continuum level. The fundamental reason is multiscale order: as active degrees of freedom fail to percolate the system, microscopic nonreciprocity cannot upscale to the continuum, instead remaining trapped in optical modes and high wave numbers. We anticipate our results to apply broadly to active solids upon sufficient dilution [9,11–13,45,47,52], and speculate that active percolation transitions radically affect core functional properties of such materials such as soliton propagation [53], synchronization [10,12], locomotion, or learning [42–44,54], as well as offering enhanced mechanical tunability of nonequilibrium moduli [40,41,45,52,55,56]. Recent experiments directly probe the structure-function link in biologically active solids, measuring nonreciprocal moduli in epithelia [57] alongside acoustic and optical modes in active spinners [47]. Given such advances, our results suggest correlating the distribution of active elements with measurements of mode structure as a useful quantifier for active response in living systems, just as structural connectivity data predicts passive rigidity in cell networks [58].

The phenomena we uncover here are also reminiscent of recent work on vanishing nonreciprocity upon coarse-graining active fluids [35], albeit with a distinct physical mechanism. This commonality invites the question of a fluidic analogue to the percolation of active units [59], and highlights the subtleties of predicting the large-scale properties of active networks: our results form an amusing analog to Braess' paradox [60,61], in which adding more roads to a network increases travel times, or indeed adding more struts to a bridge makes it weaker. Recent analogs to active matter in quantum and optomechanical platforms observe many-body synchronised states which are powered by nonreciprocity [19,22]. An exciting future question is to ask whether an analogous active percolation transition exists in this quantum context.

ACKNOWLEDGMENTS

We thank Edan Lerner and Moumita Das for helpful discussions. J. B. acknowledges funding from the European Union's Horizon research and innovation programme under the Marie Sklodowska-Curie Grant Agreement No. 101106500. C. C. and J. V. acknowledge funding from the European Research Council under Grant Agreement No. ERC-StG 852587. C. C. acknowledges funding from the Netherlands Organization for Scientific Research under Grant Agreement No. VI.Vidi.213.131 and from the European Research Council under Grant Agreement No. ERC-CoG 101170693. A. S. acknowledges funding from UKRI through Award No. EP/T000961/1. This research was supported in part by Grant No. NSF PHY-2309135 to the Kavli Institute for Theoretical Physics (KITP) and by the Dutch Institute for Emergent Phenomena (DIEP).

DATA AVAILABILITY

The data that support the findings of this article are openly available [63].

APPENDIX A: SUMMARY OF RESULTS

In this Appendix, in Secs. II and III we develop the general framework for constructing dynamical matrices of

nonreciprocal lattices and coarse graining to extract elastic moduli. In Sec. IV we give an argument demonstrating that the link between microscale stiffness and macroscale elasticity must be monotonic for passive materials, and give conditions on when the odd modulus K^o anomalously vanishes. Section V shows how active force chains vanish in our honeycomb metamaterials. Section VI describes the computational implementation of our analytical calculations and the numerical methods we use to analyze periodic and random ball-spring lattices. Finally, Secs. IX and X provide experimental details for the construction of our robotic metamaterials and experimental protocols.

APPENDIX B: FROM MICROSCOPICS TO THE ELASTIC LIMIT FOR NONRECIPROCAL LATTICES

In this section we describe how to construct the dynamical matrix for an arbitrary network containing nonreciprocal active bonds, and how to coarse-grain this matrix to extract elastic moduli. Our approach follows [38,62] generalized to include the nonreciprocal force laws described in the main text.

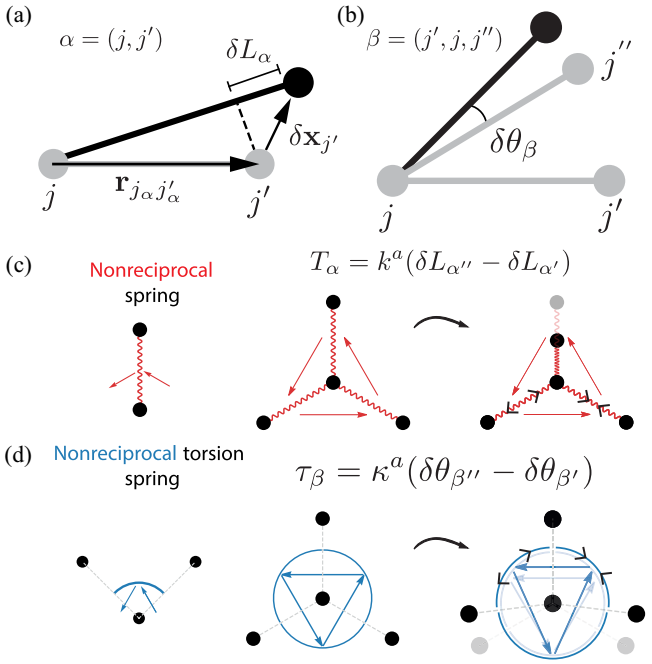


FIG. 5. (a),(b) Schematics of the variables associated with the αth longitudinal spring given by the ball-index pair $[j_\alpha, j'_\alpha]$ and the βth torsional spring given by the ball-index triplet $[j'_\beta, j_\beta, j''_\beta]$. (c),(d) Schematics of nonreciprocal tension-length springs and torsion-angle springs. The connectivity network that encodes neighboring lengths (angles) is shown via red (blue) arrows. In each panel we show an example deformation, with the corresponding longitudinal (angular) tensions shown as black arrows.

1. Nonreciprocal lattices

A lattice is described by a set of balls (labeled $j = 1, 2, \ldots$), and a set of springs connecting these balls. Here we consider two types of spring: longitudinal and torsional. Each longitudinal spring (labeled $\alpha = 1, 2, \ldots$) identifies an ordered pair of ball indices $[j_\alpha, j'_\alpha]$, and each torsional spring (labeled $\beta = 1, 2, \ldots$) identifies an ordered triple of ball indices $[j'_\beta, j_\beta, j''_\beta]$, as shown in Figs. 5(a) and 5(b).

A longitudinal spring α has a length change δL_α and linear tension T_α. A torsional spring β has an angle change $\delta\theta_\beta$ and angular tension (or torque) τ_β. Here, the angle subtended by this torsional bond is defined in a right-handed (counterclockwise) sense, in other words from j' to j'' about j in Fig. 5(b). In Eq. (B8) below we will prescribe nonreciprocal relations between the length and angle changes and tensions.

Within this framework, the linearized map between ball displacements $\delta\boldsymbol{X} = (\delta\boldsymbol{x}_1^\intercal, \delta\boldsymbol{x}_2^\intercal, \ldots)^\intercal$ and ball forces $\boldsymbol{F} = (\boldsymbol{f}_1^\intercal, \boldsymbol{f}_2^\intercal, \ldots)^\intercal$ can be written as

$$M\delta\ddot{\boldsymbol{X}} = \boldsymbol{F} = -D\delta\boldsymbol{X} = -C^\intercal \Bbbk C\delta\boldsymbol{X}, \tag{B1}$$

where $M = \mathrm{diag}(m_1, m_2, \ldots)$ is the matrix of ball masses. The dynamical matrix D splits into three separate matrices,

$$D = C^\intercal \Bbbk C. \tag{B2}$$

First, the compatibility matrix C maps ball displacements $\delta\boldsymbol{X}$ to bond elongations $\delta\boldsymbol{E} = (\delta\boldsymbol{L}^\intercal, \delta\boldsymbol{\theta}^\intercal)^\intercal = (\delta L_1, \delta L_2, \ldots, \delta\theta_1, \delta\theta_2, \ldots.)^\intercal$. For a lattice composed of both longitudinal and torsional springs, C splits into a longitudinal part, C_L and a torsional part C_θ, with

$$\delta\boldsymbol{E} = \begin{pmatrix} \delta L \\ \delta\theta \end{pmatrix} = \begin{pmatrix} C_L \\ C_\theta \end{pmatrix} \delta\boldsymbol{X} = C\delta\boldsymbol{X}. \tag{B3}$$

We will give explicit constructions of C_L and C_θ in Sec. B 3. Next, the connectivity matrix $\Bbbk$ maps elongations $\delta\boldsymbol{E}$ to tensions $\boldsymbol{T} = (T_1, T_2, \ldots, \tau_1, \tau_1, \ldots)^\intercal$

$$\boldsymbol{T} = -\Bbbk\delta\boldsymbol{E}, \tag{B4}$$

such that (for positive diagonal entries in $\Bbbk$) an change in elongation leads to a tension that opposes that elongation. We will discuss more exotic constructions of $\Bbbk$ in Sec. B 2. Finally the equilibrium matrix $C^\intercal$ maps tensions to forces

$$\boldsymbol{F} = C^\intercal\boldsymbol{T}. \tag{B5}$$

2. The microscopic stiffness matrix $\Bbbk$

In a standard ball-spring lattice made up of Hookean longitudinal and torsional springs, $\Bbbk$ would simply be a

diagonal matrix of spring constants, $\mathbb{k} = \mathrm{diag}(k_1, k_2, \ldots, \kappa_1/a^2, \kappa_2/a^2, \ldots)$, where the k_α and κ_β are the longitudinal and torsional spring constants and a is a typical length scale of the lattice. More generally, whenever spring couplings are derived from a potential, $\mathbb{k}$ is constrained to be symmetric.

Our lattices break this reciprocal symmetry by explicitly including an antisymmetric component in $\mathbb{k}$,

$$\mathbb{k} = \begin{pmatrix} \vdots & \ddots & \vdots & & \vdots & \\ \ldots & k^a & \ldots & k & \ldots & -k^a & \ldots \\ \vdots & & \vdots & \ddots & \vdots & \end{pmatrix}. \quad \text{(B6)}$$

The microscopic spring stiffness matrix $\mathbb{k}$ encodes information sharing between different springs: If $\mathbb{k}$ contains nondiagonal elements, elongations in one spring can generate tensions in another spring. Interpreting $\mathbb{k}$ as a graph-theoretical adjacency matrix for this interspring communication network, the antisymmetric component corresponds to directed cycles within this network. Figure 5(c) shows a minimal example of this network: a length three cycle connecting extensional springs, with the connectivity network shown as directed red arrows. Figure 5(d) shows a similar example for torsional springs. For any cycle of extensional springs $(\ldots\alpha', \alpha, \alpha'', \ldots)$ or torsional springs $(\ldots\beta', \beta, \beta'', \ldots)$ we then have the force laws

$$T_\alpha = k^a(\delta L_{\alpha''} - \delta L_{\alpha'}), \quad \text{(B7)}$$

$$\tau_\beta = \kappa^a(\delta\theta_{\beta''} - \delta\theta_{\beta'}), \quad \text{(B8)}$$

with the corresponding entries in $\mathbb{k}$ reading $\mathbb{k}_{\alpha\alpha''} = -\mathbb{k}_{\alpha\alpha'} = k^a$, $\mathbb{k}_{\beta\beta''} = -\mathbb{k}_{\beta\beta'} = \kappa^a$.

3. The compatibility matrix C

Given an arrangement of springs, and relative ball positions $\boldsymbol{r}_{jj'}$ as shown in Figs. 5(a) and 5(b), the expressions for the elements of C follow from direct geometric calculations of linearized length and angle changes for longitudinal and torsional springs in terms of ball displacements. The displacement of a single extensional spring $\alpha = [j_\alpha, j'_\alpha]$ gives a linearized length change δL_α of

$$\delta L_\alpha = \begin{pmatrix} -\hat{\boldsymbol{r}}_{jj'} & \hat{\boldsymbol{r}}_{jj'} \end{pmatrix} \begin{pmatrix} \delta\boldsymbol{x}_j \\ \delta\boldsymbol{x}_{j'} \end{pmatrix}, \quad \text{(B9)}$$

as shown in Fig. 5(a). In Eq. (B9) $\hat{\boldsymbol{r}}$ denotes the normalized bond vector $\boldsymbol{r}$, and we omit the spring-index subscripts α when they are clear from context. Similarly, the displacement of a single torsional spring $\beta = [j'_\beta, j_\beta, j''_\beta]$ [Fig. 5(b)] gives a linearized angle change $\delta\theta_\beta$ of

$$\delta\theta_\beta = \begin{pmatrix} -\frac{\hat{\boldsymbol{r}}^\perp_{jj'}}{r_{jj'}} & \frac{\hat{\boldsymbol{r}}^\perp_{jj'}}{r_{jj'}} - \frac{\hat{\boldsymbol{r}}^\perp_{jj''}}{r_{jj''}} & \frac{\hat{\boldsymbol{r}}^\perp_{jj''}}{r_{jj''}} \end{pmatrix} \begin{pmatrix} \delta\boldsymbol{x}_{j'} \\ \delta\boldsymbol{x}_j \\ \delta\boldsymbol{x}_{j''} \end{pmatrix}, \quad \text{(B10)}$$

where $\boldsymbol{r}^\perp = \hat{\boldsymbol{z}} \times \boldsymbol{r}$ gives a counterclockwise (right-handed) rotation, and $r = |\boldsymbol{r}|$. From these relations we build the compatibility matrix row by row. The αth row of C_L is given by

$$(C_L)_\alpha = (\boldsymbol{e}_{j'_\alpha} - \boldsymbol{e}_{j_\alpha}) \otimes \boldsymbol{r}_{j_\alpha j'_\alpha}, \quad \text{(B11)}$$

where $\boldsymbol{e}_j$ is a row vector with a 1 in position j, and zeros elsewhere (more formally $\boldsymbol{e}_j$ is a dual vector on the space of ball displacements). Here, $\otimes$ is the Kronecker product between row vectors, i.e., $(u_1, u_2, \ldots) \otimes (v_1, v_2, \ldots) = (u_1 v_1, u_1 v_2, \ldots, u_2 v_1, u_2 v_2, \ldots)$. In a similar fashion, for a torsional bond β we have

$$(C_\theta)_\beta = (\boldsymbol{e}_{j''_\beta} - \boldsymbol{e}_{j_\beta}) \otimes \frac{\hat{\boldsymbol{r}}^\perp_{j_\beta j''_\beta}}{r_{j_\beta j''_\beta}} - (\boldsymbol{e}_{j'_\beta} - \boldsymbol{e}_{j_\beta}) \otimes \frac{\hat{\boldsymbol{r}}^\perp_{j_\beta j'_\beta}}{r_{j_\beta j'_\beta}}. \quad \text{(B12)}$$

4. Periodic lattices

The expressions given above apply to any network of balls and springs, periodic or not. We now specialize to periodic lattices. In a two-dimensional periodic lattice with primitive vectors $\boldsymbol{a}_1, \boldsymbol{a}_2$ a single ball is no longer indexed by an integer j but by the pair $(j, \boldsymbol{\ell})$, where the lattice index $\boldsymbol{\ell} \in \mathbb{Z}^2$ enumerates the unit cells, and the basis index $j = 1 \cdots N$ enumerates the N balls within the unit cell. The equilibrium positions of balls are $\boldsymbol{x}_{j,\boldsymbol{\ell}} = \boldsymbol{x}_{j,0} + \boldsymbol{R}(\boldsymbol{\ell})$, in terms of a lattice vector $\boldsymbol{R}(\boldsymbol{\ell}) = \ell_1\boldsymbol{a}_1 + \ell_2\boldsymbol{a}_2$ and a position $\boldsymbol{x}_{j,\boldsymbol{0}}$ of the jth ball in the central ($\boldsymbol{\ell} = \boldsymbol{0}$) unit cell. Similarly to ball indices, we now enumerate the longitudinal spring which connects balls $(j_\alpha, \boldsymbol{\ell}_\alpha + \boldsymbol{\ell})$ and $(j'_\alpha, \boldsymbol{\ell}'_\alpha + \boldsymbol{\ell})$ with the pair $(\alpha, \boldsymbol{\ell})$. With the same notation, the torsional spring indexed by $(\beta, \boldsymbol{\ell})$ subtends the counterclockwise angle between balls $(j'_\beta, \boldsymbol{\ell}'_\beta + \boldsymbol{\ell})$ to $(j''_\beta, \boldsymbol{\ell}''_\beta + \boldsymbol{\ell})$ about the ball $(j_\beta, \boldsymbol{\ell}_\beta + \boldsymbol{\ell})$.

If the dynamics implemented by the connectivity matrix $\mathbb{k}$ satisfy the lattice periodicity, we can always assign the springs to the unit cell such that each active spring only communicates with active springs within the same unit cell, that is $\mathbb{k}_{(\alpha,\boldsymbol{\ell}),(\alpha',\boldsymbol{\ell}')} = \mathbb{k}_{\alpha\alpha'}\delta_{\boldsymbol{\ell}\boldsymbol{\ell}'}$.

With this preparation, the dynamical equation Eq. (B1) for the periodic lattice can be written as

$$\boldsymbol{F}_\ell = -\sum_{\ell'} D_{\ell'}\delta\boldsymbol{X}_{\boldsymbol{\ell}+\boldsymbol{\ell}'}, \qquad D_{\ell'} = \sum_{\boldsymbol{\ell}} C^{\mathsf{T}}_{\boldsymbol{\ell}}\mathbb{k}C_{\boldsymbol{\ell}+\boldsymbol{\ell}'}, \quad \text{(B13)}$$

where we have used periodicity to define the $\boldsymbol{\ell}$-parametrized family of compatibility matrices

$$C_{\boldsymbol{\ell}} \coloneqq \frac{\delta\boldsymbol{E}_{\boldsymbol{0}}}{\delta\boldsymbol{X}_{\boldsymbol{\ell}}} = \frac{\delta\boldsymbol{E}_{\ell'}}{\delta\boldsymbol{X}_{\boldsymbol{\ell}+\boldsymbol{\ell}'}} \quad \forall\, \ell'. \quad \text{(B14)}$$

We re-write these expressions in terms of Bloch coefficients $\delta \boldsymbol{X}(\boldsymbol{q}) = \sum_{\boldsymbol{\ell}} \delta \boldsymbol{X}_{\boldsymbol{\ell}} e^{-i\boldsymbol{q}\cdot\boldsymbol{R}(\boldsymbol{\ell})}$ with wave-vector $\boldsymbol{q}$. Taking the Fourier transform of Eq. (B13), we obtain

$$\boldsymbol{f}(\boldsymbol{q}) = -D(\boldsymbol{q})\delta\boldsymbol{X}(\boldsymbol{q}) = -C(\boldsymbol{q})^{\dagger}\mathbb{k}C(\boldsymbol{q})\delta\boldsymbol{X}(\boldsymbol{q}), \tag{B15}$$

where the Bloch compatibility matrix is

$$C(\boldsymbol{q}) = \sum_{\boldsymbol{\ell}} \frac{\delta \boldsymbol{E}_{\boldsymbol{0}}}{\delta \boldsymbol{X}_{\boldsymbol{\ell}}} e^{i\boldsymbol{q}\cdot\boldsymbol{R}(\boldsymbol{\ell})} = \frac{\delta}{\delta \boldsymbol{X}(\boldsymbol{q})} \begin{pmatrix} \boldsymbol{L}_{\boldsymbol{0}} \\ \boldsymbol{\theta}_{\boldsymbol{0}} \end{pmatrix}. \tag{B16}$$

Explicit row-wise expressions for elements of the $\boldsymbol{q}$-space compatibility matrix $C(\boldsymbol{q})$ mirror those given in Eqs. (B11), (B12), but contain additional Floquet factors when springs cross neighboring unit cells. For longitudinal springs,

$$\begin{aligned}(C_L)_{\alpha} &= \frac{\delta L_{\alpha,\boldsymbol{0}}}{\delta \boldsymbol{X}(\boldsymbol{q})} \\ &= (\boldsymbol{e}_{j'_{\alpha}} e^{i\boldsymbol{q}\cdot\boldsymbol{R}(\boldsymbol{\ell}'_{\alpha})} - \boldsymbol{e}_{j_{\alpha}} e^{i\boldsymbol{q}\cdot\boldsymbol{R}(\boldsymbol{\ell}_{\alpha})}) \otimes \hat{\boldsymbol{r}}_{j_{\alpha}\boldsymbol{\ell}_{\alpha}j'_{\alpha}\boldsymbol{\ell}'_{\alpha}},\end{aligned} \tag{B17}$$

for the αth row of $C(\boldsymbol{q})$. Similarly, for torsion springs we find

$$\begin{aligned}(C_{\theta})_{\beta} &= \frac{\delta \theta_{\beta,\boldsymbol{0}}}{\delta \boldsymbol{X}(\boldsymbol{q})} \\ &= (\boldsymbol{e}_{j''_{\beta}} e^{i\boldsymbol{q}\cdot\boldsymbol{R}(\boldsymbol{\ell}''_{\beta})} - \boldsymbol{e}_{j_{\beta}} e^{i\boldsymbol{q}\cdot\boldsymbol{R}(\boldsymbol{\ell}_{\beta})}) \otimes \frac{\hat{\boldsymbol{r}}^{\perp}_{j_{\beta}\boldsymbol{\ell}_{\beta}j''_{\beta}\boldsymbol{\ell}''_{\beta}}}{r_{j_{\beta}\boldsymbol{\ell}_{\beta}j''_{\beta}\boldsymbol{\ell}''_{\beta}}} \\ &\quad - (\boldsymbol{e}_{j'_{\beta}} e^{i\boldsymbol{q}\cdot\boldsymbol{R}(\boldsymbol{\ell}'_{\beta})} - \boldsymbol{e}_{j_{\beta}} e^{i\boldsymbol{q}\cdot\boldsymbol{R}(\boldsymbol{\ell}_{\beta})}) \otimes \frac{\hat{\boldsymbol{r}}^{\perp}_{j_{\beta}\boldsymbol{\ell}_{\beta}j'_{\beta}\boldsymbol{\ell}'_{\beta}}}{r_{j_{\beta}\boldsymbol{\ell}_{\beta}j'_{\beta}\boldsymbol{\ell}'_{\beta}}}.\end{aligned} \tag{B18}$$

5. Coarse-graining procedure

We now describe how to take the dynamical matrix $D(\boldsymbol{q}) = C(\boldsymbol{q})^{\dagger}\mathbb{k}C(\boldsymbol{q})$ from Eq. (B15), and coarse grain to extract elastic moduli. The approach is to separate displacement fields into slow and fast variables. The slow variable is the center-of-mass coordinate of each unit cell. The fast variables are then relative displacement vectors inside each unit cell. We will assume that these internal degrees of freedom relax on a timescale much shorter than the dynamics of the center-of-mass coordinate.

The key observation is that the kernel of $C(\boldsymbol{0})$ naturally defines the slow vibrational modes of the lattice [62]. That is, for deformation-dependent lattices, $\mathrm{Ker}[C(\boldsymbol{0})]$ always contains the uniform translations:

$$C(\boldsymbol{0})\mathbb{1} = 0 \quad \text{where } \mathbb{1} = (\boldsymbol{b}_1, \boldsymbol{b}_2) = \frac{1}{\sqrt{N}} \begin{pmatrix} 1 & 0 \\ 0 & 1 \\ 1 & 0 \\ 0 & 1 \\ \vdots & \vdots \end{pmatrix}. \tag{B19}$$

The vectors $\boldsymbol{b}_i$ span the space of rigid-body translations of masses along the $d = 2$ spatial dimensions, which keep all lengths and angles invariant. In the following derivation we assume that there are no additional zero modes beyond these two translations.

We may use the right-singular eigenvectors to split the space of ball displacements:

$$C(\boldsymbol{0})^{\dagger}C(\boldsymbol{0}) = W\Sigma^2 W^{\dagger}, \qquad W = (\,\mathbb{1} \quad V\,), \tag{B20}$$

where Σ is the diagonal matrix of right-singular values, and $W \in \mathrm{SO}(2N)$. The first two right-singular vectors in W form the block $\mathbb{1}$ spanning the kernel of $C(\boldsymbol{0})$. The remaining columns form a $2N \times (2N-2)$ matrix V and span the orthogonal complement to the kernel.

The basis change W decomposes the space of ball displacements $\delta\boldsymbol{X}(\boldsymbol{q})$ and forces $\boldsymbol{f}(\boldsymbol{q})$ as

$$\begin{pmatrix} \boldsymbol{u}(\boldsymbol{q}) \\ \boldsymbol{v}(\boldsymbol{q}) \end{pmatrix} = W^{\dagger}\delta\boldsymbol{X}(\boldsymbol{q}), \quad m\begin{pmatrix} \ddot{\boldsymbol{u}}(\boldsymbol{q}) \\ \ddot{\boldsymbol{v}}(\boldsymbol{q}) \end{pmatrix} = W^{\dagger}\boldsymbol{f}(\boldsymbol{q}), \tag{B21}$$

into a center-of-mass-like coordinate

$$\boldsymbol{u}(\boldsymbol{q}) = \mathbb{1}^{\dagger}\delta\boldsymbol{X}(\boldsymbol{q}) = \frac{\delta\boldsymbol{x}_1(\boldsymbol{q}) + \cdots + \delta\boldsymbol{x}_N(\boldsymbol{q})}{\sqrt{N}} \tag{B22}$$

and a vector of $2(N-1)$ internal displacements $\boldsymbol{v}(\boldsymbol{q})$, which we will proceed to eliminate. The square root normalization ensures orthonormality of the basis defined by W. Once we have a linear equation in $\boldsymbol{u}$ only, we can rescale it by a further $\sqrt{N}$ and treat $\boldsymbol{u}(\boldsymbol{q})$ as the Fourier components of the average motion of the unit cells. In our new basis, the dynamical equation, Eq. (B15), reads

$$m\begin{pmatrix} \ddot{\boldsymbol{u}} \\ \ddot{\boldsymbol{v}} \end{pmatrix} = -\begin{pmatrix} C_u^{\dagger}\mathbb{k}C_u & C_u^{\dagger}\mathbb{k}C_v \\ C_v^{\dagger}\mathbb{k}C_u & C_v^{\dagger}\mathbb{k}C_v \end{pmatrix}\begin{pmatrix} \boldsymbol{u} \\ \boldsymbol{v} \end{pmatrix}, \tag{B23}$$

where we have denoted $C_u(\boldsymbol{q}) = C(\boldsymbol{q})\mathbb{1}$ and $C_v(\boldsymbol{q}) = C(\boldsymbol{q})V$, and suppressed explicit $\boldsymbol{q}$ dependence for compactness.

To take the elastic limit, we consider the lowest order-expansion in the wave-vector $\boldsymbol{q}$. Note that, since the columns of $\mathbb{1}$ span the kernel of $C(\boldsymbol{0})$, $C_u \sim O(q)$, and $C_v \sim \mathrm{O}(1)$. Hence the top-left block in Eq. (B23) is $\mathrm{O}(q^2)$, and tracks long-wavelength deformations of the center of-mass coordinate. By contrast, the bottom-right block is O(1), and tracks internal modes within a unit cell.

We now eliminate the fast degree of freedom $\boldsymbol{v}(\boldsymbol{q})$, by assuming the O(1) lattice dynamics relax forces until internal forces balance, i.e., $\ddot{\boldsymbol{v}}(\boldsymbol{q}) = 0$. This assumption lets us solve for a quasistatic $\boldsymbol{v}(\boldsymbol{q})$:

$$\boldsymbol{v} = -[C_v^{\dagger}\mathbb{k}C_v]^{-1}C_v^{\dagger}\mathbb{k}C_u\boldsymbol{u}. \tag{B24}$$

Substituting $\boldsymbol{v}(\boldsymbol{q})$ from Eq. (B24) back into the force-displacement relation Eq. (B23) we obtain the dynamical equation for the center-of-mass coordinate

$$\rho\ddot{\boldsymbol{u}} = -\frac{N}{\mathcal{A}} C_u^\dagger (\mathbb{k} - \mathbb{k}C_v[C_v^\dagger \mathbb{k} C_v]^{-1} C_v^\dagger \mathbb{k}) C_u \boldsymbol{u}, \tag{B25}$$

where $\rho = Nm/\mathcal{A}$ is the mass density in terms of the unit cell area $\mathcal{A} = |\boldsymbol{a}_1 \times \boldsymbol{a}_2|$. Note that to lowest order in q, the entire expression within the round brackets is $O(1)$, and, in particular, the expression in square brackets is invertible at $\boldsymbol{q} = \boldsymbol{0}$.

Equation (B25) represents a coarse-grained force-displacement relation that only tracks the slow mode $\boldsymbol{u}(\boldsymbol{q})$: we have eliminated internal degrees of freedom and coarse grained to an effectively affine lattice from which we may extract elastic moduli.

APPENDIX C: ELASTIC MODULI

In this section we describe how to extract elastic moduli from the coarse-grained force-displacement relation, with particular attention to the linearly isotropic case. We also show how to identify the even and odd shear moduli in the linearly anisotropic case, by extending the definition of principal axes into the active domain.

1. Extracting the elastic moduli

The coarse-grained dynamical equation Eq. (B25) is (to lowest order) quadratic in $\boldsymbol{q}$, thus its Fourier transform is a second-order PDE in $\boldsymbol{u}$. For linearly isotropic materials (in particular for random lattices or periodic lattices with three-fold rotational symmetry), Ref. [38] showed by symmetry arguments that this PDE must take the form of the active Navier-Cauchy equation

$$\rho\ddot{\boldsymbol{u}} = \begin{pmatrix} B & -A \\ A & B \end{pmatrix} \boldsymbol{\nabla}(\boldsymbol{\nabla}\cdot\boldsymbol{u}) + \begin{pmatrix} \mu & -K^o \\ K^o & \mu \end{pmatrix} \nabla^2 \boldsymbol{u}, \tag{C1}$$

in terms of two passive moduli, the bulk B and shear μ moduli, alongside two active moduli, the compression-torque A and odd K^o moduli.

Accordingly, we obtain Hooke's law for active isotropic media, which relates the induced stresses $\rho\ddot{u}_i = \partial_j \sigma_{ij}$ to the imposed strain $\varepsilon_{ij} = \frac{1}{2}(\partial_i u_j + \partial_j u_i)$

$$\underline{\sigma} = 2\begin{pmatrix} B & -A \\ A & B \end{pmatrix} \mathrm{vol}(\underline{\varepsilon}) + 2\begin{pmatrix} \mu & -K^o \\ K^o & \mu \end{pmatrix} \mathrm{dev}(\underline{\varepsilon}) \tag{C2}$$

in terms of the volumetric $\mathrm{vol}(\underline{\varepsilon}) = \frac{1}{2}\mathrm{tr}(\underline{\varepsilon})I_2$ and deviatoric $\mathrm{dev}(\underline{\varepsilon}) = \underline{\varepsilon} - \mathrm{vol}(\underline{\varepsilon})$ strain tensors.

In more generality, the stress-strain relation can be written as $\sigma_{ij} = K_{ijkl}\varepsilon_{kl}$ in terms of a stiffness tensor K. Comparing with Eq. (B25), we find that the stiffness tensor is

$$K_{i\alpha j\beta} = \frac{N}{\mathcal{A}}\left[\frac{\partial (C\boldsymbol{b}_i)^\dagger}{\partial q_\alpha} \tilde{\mathbb{k}} \frac{\partial (C\boldsymbol{b}_j)}{\partial q_\beta}\right]_{\boldsymbol{q}=\boldsymbol{0}} + \epsilon_{\alpha\beta}\chi_{ij}, \tag{C3}$$

where $\epsilon_{\alpha\beta}$ is the Levi-Civita symbol, the χ_{ij} are constants of integration set by imposing boundary conditions on the stress, and the effective microscopic stiffness matrix is

$$\tilde{\mathbb{k}} = [\mathbb{k} - \mathbb{k}CV[(CV)^\dagger \mathbb{k} CV]^{-1}(CV)^\dagger \mathbb{k}]_{\boldsymbol{q}=\boldsymbol{0}}. \tag{C4}$$

From Eqs. (C3)–(C4) we can see the major symmetry of K follows directly from the symmetry of $\mathbb{k}$.

Here, we use the symmetrized strain tensor ε without loss of generality, since the microscopic dynamics are invariant under rigid rotations. Further, since uniform scaling keeps angles invariant and induces no length differences in pairs of springs that have the same rest length, B and A are independent of activity for all lattices mentioned in the main text (in particular, this means that $A = 0$). Therefore, all activity is contained in the shear response of the lattice.

2. Anisotropy and principal axes

By measuring a single arbitrary shear response, a shear-active isotropic material is indistinguishable from a passive anisotropic material. To mark the difference, we briefly mention how to identify active shear in anisotropic materials.

The elasticity tensor is a linear operation on the vector space of 2×2 matrices. We will parametrize this vector space by four matrices that represent dilation, rotation, and two shears whose axes differ by a 45° angle (Fig. 6):

$$\underline{\varepsilon} = \varepsilon_\odot \begin{pmatrix} 1 & 0 \\ 0 & 1 \end{pmatrix} + \varepsilon_\circlearrowleft \begin{pmatrix} 0 & -1 \\ 1 & 0 \end{pmatrix} + \varepsilon_+ \begin{pmatrix} 1 & 0 \\ 0 & -1 \end{pmatrix} + \varepsilon_\times \begin{pmatrix} 0 & 1 \\ 1 & 0 \end{pmatrix}. \tag{C5}$$

Similarly decomposing the stress tensor, we can collect the coefficients as vectors

$$\boldsymbol{\varepsilon} = (\varepsilon_\odot, \varepsilon_\circlearrowleft, \varepsilon_+, \varepsilon_\times)^T, \qquad \boldsymbol{\sigma} = (\sigma_\odot, \sigma_\circlearrowleft, \sigma_+, \sigma_\times)^T. \tag{C6}$$

In this basis, the stress-strain relation is $\boldsymbol{\sigma} = K\boldsymbol{\varepsilon}$ in terms of an elasticity matrix K. Since $\underline{\varepsilon}$ is symmetric by definition,

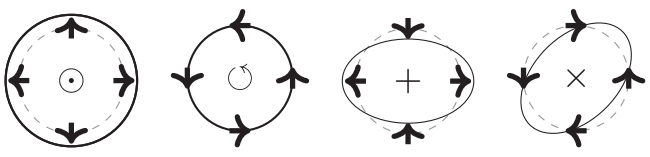


FIG. 6. The basis of linear deformations corresponding to the matrices in Eq. (C5). The arrows represent the deformations $\boldsymbol{u} = \underline{\varepsilon}\boldsymbol{x}$ or traction forces $\boldsymbol{f} = \underline{\sigma}\hat{\boldsymbol{n}}$.

$\varepsilon_{\circlearrowleft}$ is always zero. This is reflected by fixing the constant of integration χ such that the second column of K is zero.

For simplicity, let us assume shear and bulk modes are decoupled, so we can focus on the shear sector in isolation. We may rotate space until the symmetric part of K diagonalizes, and the shear stress-strain relation takes the canonical form

$$\begin{pmatrix}\sigma_+\\ \sigma_\times\end{pmatrix}=\begin{pmatrix}\mu_1 & -K^o\\ K^o & \mu_2\end{pmatrix}\begin{pmatrix}\varepsilon_+\\ \varepsilon_\times\end{pmatrix}, \tag{C7}$$

with two even (shear) moduli $\mu_{1,2}$ and one odd (shear) modulus K^o.

We will consider uniaxial compression along a varying angle φ, i.e.,

$$\underline{\varepsilon}=\varepsilon(\hat{\boldsymbol{n}}\hat{\boldsymbol{n}}^\intercal-\hat{\boldsymbol{n}}_\perp\hat{\boldsymbol{n}}_\perp^\intercal), \tag{C8}$$

where $\hat{\boldsymbol{n}}=(\cos\varphi,\sin\varphi)^\intercal$ and $\hat{\boldsymbol{n}}_\perp=(-\sin\varphi,\cos\varphi)^\intercal$. As we change the angle φ of the shear axis, we will keep track of the normal $f_\parallel$ and tangential $f_\perp$ components of the induced force at the contact plane

$$\boldsymbol{f}=\underline{\sigma}\cdot\hat{\boldsymbol{n}}=\epsilon(f_\parallel\hat{\boldsymbol{n}}+f_\perp\hat{\boldsymbol{n}}_\perp). \tag{C9}$$

Using Eq. (C7), we find

$$f_\parallel=\frac{1}{2}(\mu_1+\mu_2)+\frac{1}{2}(\mu_1-\mu_2)\cos(4\varphi), \tag{C10}$$

$$f_\perp=K^o-\frac{1}{2}(\mu_1-\mu_2)\sin(4\varphi). \tag{C11}$$

We note that $\mu_{1,2}$ and K^o are respectively the extrema of $f_\parallel$ and the average of $f_\perp$.

We thus find that one can measure the active shear modulus statically by measuring the tangential force resulting from compression along a principal axis, which for active elastic solids we may define as an axis under which the normal force is extremal. For passive materials, we recover that principal axes are characterized by a vanishing tangential force, as $f_\perp$ averages to zero if $K^o=0$. Finally, in linearly isotropic (active) materials $\mu_1=\mu_2$, and every axis is principal.

APPENDIX D: BROKEN AND PRESERVED MONOTONICITY

In this section, we provide a short proof for the monotonic relationship between microscopic stiffness and macroscopic rigidity in passive materials, and give mathematical intuition behind the nonmonotonicity that can arise in active materials.

1. Passive monotonicity

For passive solids, the stiffness matrix $\mathbb{k}$ is symmetric, allowing the force-displacement relation

$$\boldsymbol{F}=-C^\intercal\mathbb{k}\delta\boldsymbol{L}=-C^\intercal\mathbb{k}C\delta\boldsymbol{X}+O^2(\delta\boldsymbol{X}), \tag{D1}$$

to be derived as the gradient of a potential energy

$$\mathcal{E}(\delta\boldsymbol{X})=\frac{1}{2}(C\delta\boldsymbol{X})^\intercal\mathbb{k}(C\delta\boldsymbol{X})+O^3(\delta\boldsymbol{X}). \tag{D2}$$

Because we have a potential energy, we can follow a more direct coarse-graining procedure. In equilibrium, the coarse-grained free energy of an affine deformation $\boldsymbol{\varepsilon}$,

$$\mathcal{F}(\boldsymbol{\varepsilon})=\min_{\Omega(\boldsymbol{\varepsilon})}\mathcal{E}(\delta\boldsymbol{X})=\frac{1}{2}\boldsymbol{\varepsilon}^\intercal K\boldsymbol{\varepsilon}+O^3(\boldsymbol{\varepsilon}), \tag{D3}$$

is the minimum of the energy over the affine space of ball displacements that can express this deformation. For periodic lattices, we can characterize this space as

$$\Omega(\boldsymbol{\varepsilon})=\{\delta\boldsymbol{X}:\boldsymbol{u}_{\boldsymbol{\ell}}=\underline{\varepsilon}\boldsymbol{R}(\boldsymbol{\ell})\}, \tag{D4}$$

possibly augmented by other restrictions (such as the bond incompressibility in our hexagonal lattice). Here, $\boldsymbol{u}_{\boldsymbol{\ell}}=(1/N)\sum_j\delta\boldsymbol{X}_{j,\boldsymbol{\ell}}$ is the average motion of the $\boldsymbol{\ell}$th unit cell, and $\boldsymbol{R}(\boldsymbol{\ell})=\ell_1\boldsymbol{a}_1+\ell_2\boldsymbol{a}_2$ the $\boldsymbol{\ell}$th lattice vector. Note that $\Omega(\boldsymbol{\varepsilon})$ is an affine rather than linear space [in particular, $\boldsymbol{0}\notin\Omega(\boldsymbol{\varepsilon})$ for nonzero ε].

Now let us consider two scenarios (distinguished by subscripts 1 and 2) between which we increase the local stiffnesses. We use notation $K_1\le K_2$ to mean that K_2-K_2 is positive nonsemidefinite, or equivalently that the eigenvalues of K_2-K_1 are all non-negative.

Theorem IV.1. $\mathbb{k}_1\le\mathbb{k}_2\Rightarrow K_1\le K_2$.

Proof. Assume that $\mathbb{k}_2-\mathbb{k}_1$ is positive semidefinite. This is equivalent to the statement that $\mathcal{E}_1(\delta\boldsymbol{X})\le\mathcal{E}_2(\delta\boldsymbol{X})$ for all $\delta\boldsymbol{X}$. It suffices to show that $\mathcal{F}_1(\boldsymbol{\varepsilon})\le\mathcal{F}_2(\boldsymbol{\varepsilon})$ for all $\boldsymbol{\varepsilon}$. Let $\delta\boldsymbol{X}_i$ be the minimizer of $\mathcal{E}_i$ over $\Omega(\boldsymbol{\varepsilon})$, then indeed

$$\mathcal{E}_1(\delta\boldsymbol{X}_1)\le\mathcal{E}_1(\delta\boldsymbol{X}_2)\le\mathcal{E}_2(\delta\boldsymbol{X}_2), \tag{D5}$$

by minimizer and microscopic monotonicity respectively. Thus K_2-K_1 is positive semidefinite. ∎

In particular for diagonal $\mathbb{k}$, increasing any of its diagonal elements (microscopic stiffnesses) cannot decrease the eigenvalues of K (the elastic moduli).

2. High-activity nonmonoticity

At nonzero activity, we assume our lattice still finds an equilibrium state, given by the force-balance condition

$$\boldsymbol{0}=\boldsymbol{F}_p+\boldsymbol{F}_a=C^\intercal(\mathbb{k}_p+\mathbb{k}_a)C\delta\boldsymbol{X}, \tag{D6}$$

where $\mathbb{k}_p$ and $\mathbb{k}_a$ are the passive (symmetric) and active (antisymmetric) components of the microscopic stiffness matrix $\mathbb{k}$.

To explain the vanishing of K^o and stiffening of μ in underpercolated lattices, we focus at force balance in the high-activity regime. For simplicity, we restrict our attention to systems without stiff scaffolding (e.g., $\kappa \ll \kappa_a \ll k$) where the analysis would be a bit more involved, but the conclusions similar. The force-balance Eq. (D6) is then dominated by the active force, and is to first approximation satisfied by affine displacements belonging to the set

$$\Omega_a = \{\delta \boldsymbol{X} \in \Omega : \boldsymbol{F}_a = \boldsymbol{0}\} = \Omega \cap \ker(C^\intercal \mathbb{k}_a C), \quad \text{(D7)}$$

where we have suppressed $\boldsymbol{\varepsilon}$ dependence for compactness. The equilibrium displacement is given by the minimizer of the passive potential [Eq. (D2) with $\mathbb{k} = \mathbb{k}_p$] over this reduced space of active-force-balancing affine displacements Ω_a. An increase in μ indicates that the energy minimizer over $\Omega(\boldsymbol{\varepsilon})$, where $\boldsymbol{\varepsilon}$ is a shear, is no longer contained in the restricted space $\Omega_a(\boldsymbol{\varepsilon})$.

Net active forces $\boldsymbol{F}_a$ can vanish either because generated nonzero active forces balance out, or because no active forces are generated at all. In the latter case, any stress must be generated by passive elements, and therefore odd elastic moduli such as K^o must vanish. We call displacements that do not generate active forces *active floppy modes*, and analyze them as members of

$$\Omega_a^0 = \{\delta \boldsymbol{X} \in \Omega : \boldsymbol{T}_a = \boldsymbol{0}\} = \Omega \cap \ker(\mathbb{k}_a C), \quad \text{(D8)}$$

since absence of active tensions implies absence of active forces. Thus, we find that K^o must vanish if the minimum over Ω_a is contained in the subset Ω_a^0.

As we dilute the active elements in our lattice (that is, decrease the activation fraction p), the rank of $\mathbb{k}_a$ decreases. As a result, the space of active floppy modes (the kernel of $\mathbb{k}_a C$) broadens, and commensurately the space of generatable active force configurations (the image of $\mathbb{k}_a C$) shrinks. When, for a given ε, the image $\mathbb{k}_a C[\Omega(\boldsymbol{\varepsilon})]$ has shrunk to the point that it no longer intersects the kernel of $C^\intercal$, all active-force-balancing microscopic displacements that realize the macroscopic affine deformation $\boldsymbol{\varepsilon}$ must be floppy. Thus the minimum over Ω_a must be contained in Ω_a^0 (as $\Omega_a = \Omega_a^0$), and the odd moduli associated with ε must vanish.

APPENDIX E: ACTIVE FORCE BALANCE IN HONEYCOMB METAMATERIALS

In the main text, we rationalize the emergence of plaquette locking and a nonmonotonic $K^o(\kappa^a)$ in our honeycomb metamaterials by first simplifying to a triangular lattice (Fig. 3). This minimal model captures the essence of the phenomena, but here we describe the equivalent breakdown of active tension chains in our honeycomb metamaterials.

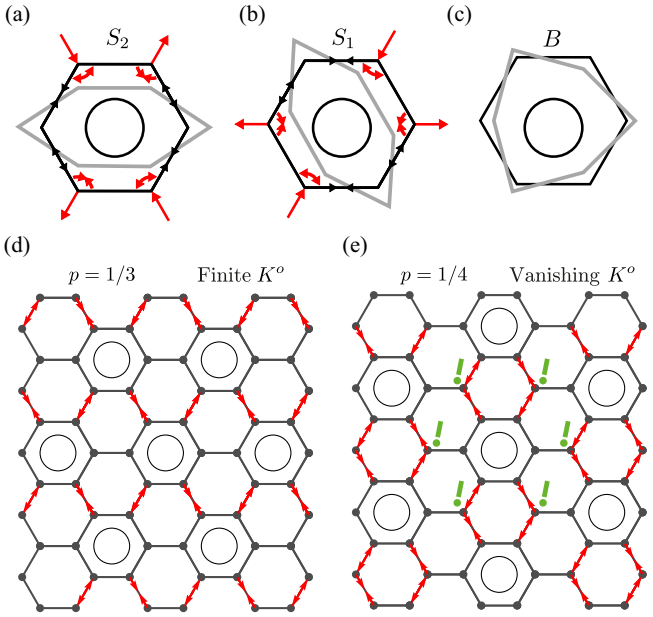


FIG. 7. Vanishing odd response in honeycomb metamaterials (a)–(c) The active forces (external thick red arrows) generated by a basis for the space of infinitesimal motions of the equilateral hexagon (shown exaggerated in gray outline), up to rotation and translation. The change in angle generates active torques (red internal arrows), which lead to forces on the vertices (thin light-red arrows), whose components along the bars (black arrows) are resisted by the incompressibility of the rigid linkages. (d) A macroscopic force chain built from these antisymmetric plaquette-level nodal forces in a $p = 1/3$ lattice. This lattice supports finite odd response at large activity. (e) In a $p = 1/4$ tiled lattice we cannot successfully construct active force chains without unbalanced nodal forces (exclamation points). This lattice cannot support K^o at high activity.

Figures 7(a)–7(c) show a basis for the deformations of an incompressible hexagon, composed of two shear modes and one breathing mode. In a nonreciprocal plaquette, these shear modes generate angular tensions [Figs. 7(a) and 7(b), red internal arrows] and hence nodal forces [Figs. 7(a) and 7(b), red external arrows] which are skewed with respect to the applied shear. The remaining breathing mode does not couple to nonreciprocity. In Figs. 7(c) and 7(d) we attempt to tile these plaquette level active forces across the two lattices shown in Figs. 2(b) and 2(c), which exhibit the transition into nonmonotonic response and plaquette locking. In Fig. 7(d) every third plaquette is active ($p = 1/3$) and our theory predicts that odd response is monotonic, $K^o = 2\kappa^a/a^2$. Note that $p = 1/3$ is actually below the $p = 1/2$ transition shown in Fig. 2(k). In this case, the specific periodic structure of the tiling nevertheless allows a finite odd response not seen in a typical random tiling. By contrast, in the more dilute lattice shown in Fig. 7(e), which is experimentally realized in Fig. 1, we have

$p = 1/4$ and we predict that odd response vanishes at large activity, Eq. (1). Analogously to the triangular lattices shown in Fig. 3, we discover that tension chains can be successfully constructed in Fig. 7(d), but they cannot in Fig. 7(e): we necessarily encounter unbalanced nodal forces [Fig. 7(e), exclamation points]. The actual force-balanced displacement fields adopted by the lattice are shown in Figs. 2(b) and 2(c).

APPENDIX F: DATA ANALYSIS AND COMPUTATIONAL METHODOLOGY

In this section we describe our computational methodology for building the dynamical matrices of lattices and extracting their elastic moduli which is used throughout the main text. We also provide details of the data analysis used to generate the visualizations shown in Fig. 1, alongside the theoretical results shown in Figs. 2–4.

1. Analysis of honeycomb lattice data

Throughout Fig. 1 we compare experimental data to theoretical predictions for honeycomb lattices. These theoretical data [curves in Figs. 1(c) and 1(f), image in Fig. 1(e)] are generated using the coarse-graining procedure leading to Eq. (1), described in Sec. II. We implement the symbolic expressions for **q**-space compatibility matrices Eqs. (B17), (B18) to generate dynamical matrices as in Eq. (B15) using *Mathematica* 12. Elastic moduli are computed through the symbolic expression Eq. (C3). In practice the symbolic inversion of $C^\dagger \mathbb{k} C$ in Eq. (C3) limits a naive analytic calculation to around 8 balls per unit cell. For larger lattices we replace analytic inversions with numerical matrix solves.

For the lattice shown in Fig. 1 we find the odd and shear moduli in Eq. (1) of the main text, with $c_1 = 27/64$, $c_2 = 45/64$. In Fig. 2 we show several progressively diluted honeycomb lattices, of which panel (c) corresponds to the lattice shown in Fig. 1(a). Analytical results for the other panels are

$$K^o = 6\kappa^a, \qquad \mu = 2\sqrt{3}\kappa \text{ panel a}, \tag{F1}$$

$$K^o = 2\kappa^a, \qquad \mu = 2\sqrt{3}\kappa \text{ panel b}, \tag{F2}$$

in units of the honeycomb side spacing $a = 1$. The unit cell of Fig. 2(d) is too large for an analytical inversion, and we proceed numerically as for random lattices.

To generate the strain fields shown in Figs. 1(e) and 1(f), we apply the simple shear ϵ to a unit cell, let the internal degrees of freedom relax [i.e. use $\boldsymbol{v}$ in Eq. (B24) for the internal ball displacements], and then compute hexagonal shear strains using Eq. (J2). In Figs. 2(a)–2(h), we instead apply a vertical pure shear for visual clarity, otherwise the procedure is identical.

2. Analysis of triangular lattice data

In Figs. 3 and 4 we consider a minimal model of a nonreciprocal lattice, composed of a triangular lattice of longitudinal springs [$T_i = -k\delta L_i$] and nonreciprocal longitudinal springs [$T_i = k^a(\delta L_{i+1} - \delta L_{i-1})$]. Our general notation for such springs is shown in Fig. 5(c), with a specific triangular building block shown in Fig. 3.

a. Eigenspectra and elastic moduli of periodic triangular lattices

Figures 4(a)–4(d) analyzes the eigenspectra for the ten isotropic dilutions of a 2×4 supercell of such triangular plaquettes. The unit cells of all such dilutions, alongside their dilution factor p and elastic moduli, are given in Table I and shown in Fig. 8. The mapping between Fig. 4 and Table I is Panel (a): $p = 8/8$ (Table I, first row). Panel (b): $p = 5/8$ (fourth row). Panel (c): $p = 3/8$ (eighth row). For all eigenspectra shown in Fig. 4, $k^a/k = 5$, and

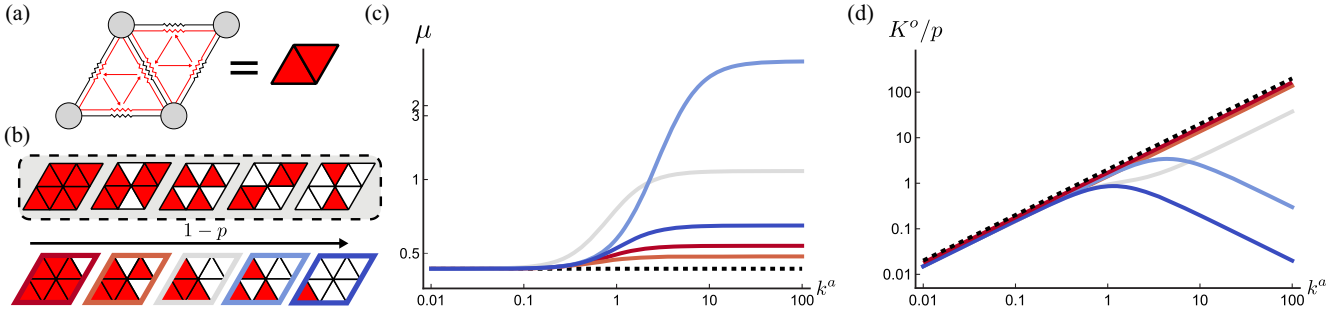


FIG. 8. Odd and shear moduli of periodic triangular active lattices (a) Sketch of periodic tile of extension-active triangles, with black passive springs with tension laws $T_{p,i} = -k\delta L_i$, and red active springs with tension laws $T_{a,i} = -k^a(\delta L_{i-1} - \delta L_{i+1})$. (b) The ten isotropic dilutions of a 4×4 triangular unit cell (table I). Colors map to the curves shown in panels (c),(d). (c),(d) Shear μ and odd K^o moduli of the ten dilutions shown in (b), as a function of k^a. We rescale K^o by p in panel (b) to collapse the monotonic lattice responses onto one another. Just as in our honeycomb lattices, the overall trend is for K^o to vanish for small p, and μ to exhibit a peak at intermediate values of p. However certain lattices defy this trend. For example, our $p = 2/8$ lattice remains monotonic despite being unpercolated, because active bonds form system-spanning chains.

the triangular lattice side length is set to $a = 1$. For the slope and gap metrics we set $k^a/k = 100$.

Note that there are several periodic dilutions all with $p = 4/8 = 1/2$, shown as gray dots in Fig. 4(d), which all have different eigenspectra and elastic moduli. We take their average to draw the line in Fig. 4(d). This diversity is a reflection of the specific spatial structure of each lattice: periodic lattices sitting on the edge of percolation thresholds (isostatic lattices) often show distinct elastic properties depending on the details of their geometry [62]. We note also that the $p = 2/8$ lattice of Table I presents an interesting edge case in which the eigenspectrum near the origin appears to scale as a power law; such edge cases are washed out in the averaging of random lattices.

In Fig. 8, we show the elastic moduli of these triangular lattices as a function of k^a—analogous curves for honeycomb lattices are shown in Figs. 2(i) and 2(j). Just as in our honeycomb lattices, the trend is for K^o to vanish as p decreases, with a spike in μ at intermediate values of p. Note, however, that certain lattices defy this trend, for example, the $p = 2/8$ lattice discussed above is underpercolated yet shows a diverging odd modulus, because plaquettes are still able to form system-spanning clusters.

b. Curve fits

To fit the slope and gap data shown in Figs. 4(d) and 4(h), we first extract a one-dimensional representation of the eigenspectrum in the complex plane by taking marginals over the $\mathrm{Re}(\omega)$ axis. For the random data, we apply a bilinear fit to the eigenspectrum lying in the upper half plane, with the $\mathrm{Re}(\omega)$ intersection of the second line a free parameter. This intersection defines the gap. For the structured data, it suffices to fit two lines separately: once to data about the origin, defining the slope, and once to the entire dataset, whose intersection with the $\mathrm{Re}(\omega)$ axis defines the gap. The error bars shown in Figs. 4(h) are obtain by fitting the gap and slope for the eigenspectrum of each sample, and then taking the mean and standard deviation of these fluctuating quantities.

c. Eigenspectra and eigenvectors of random lattices

We generate random lattices as described below. The eigenspectra plots of Fig. 4 are then density plots of all the eigenvalues ω taken from 50 realizations. The realizations of displacement fields shown in Figs. 4(i)–4(k) are a random subset of these data taken from each lobe of the spectrum for an underpercolated lattice. The shear strain in a triangular plaquette is defined as

$$S_1 = \frac{1}{\sqrt{2}}(\delta\theta_1 - \delta\theta_2) \quad \text{triangular}, \tag{F3}$$

$$S_2 = \frac{1}{\sqrt{6}}(\delta\theta_1 + \delta\theta_2 - 2\delta\theta_3) \quad \text{triangular}, \tag{F4}$$

and is visualized identically to the methodology used for honeycomb lattices.

3. Generation of random lattices

To generate the random lattices shown in Figs. 2 and 4 we generate the $\mathbf{q}$-space dynamical matrix of a periodic lattice which has the (large) unit cell that coincides with the random lattice we wish to study. We then extract elastic moduli as above. We generate these dynamical matrices by first generating the dynamical matrix of a fully tiled lattice, and then removing active plaquettes from $D(\mathbf{q})$ with a probability p to construct our randomized $D(\mathbf{q})$. In Fig. 2 we generate lattices of 25×25 honeycomb plaquettes, and in Fig. 4 we generate lattices of 40×40 triangular plaquettes. As above, the analytical inversions in Eq. (C3) are infeasible here and we use numerical matrix solves instead. In each case we generate 50 random realizations to compute statistics on—we check that this is a sufficient number of realizations for our statistics to converge. The data shown in Fig. 2 has the complication that we wish to work in the limit $k \to \infty$, however, we generate $D(\mathbf{q})$ for finite k. In practice, we generate several datasets for $k = 10^3, 10^4, 10^5$. We check that the data converges, that the condition number of $D(\boldsymbol{q})$ is acceptable for the number of digits of accuracy we require on μ and K^o, and that *Mathematica* issues no warnings on the condition number.

APPENDIX G: ODD PERCOLATION OCCURS IN POSITIONALLY DISORDERED LATTICES

In the main text we have focused on the effects of on-lattice disorder, but the percolation scenario we describe also occurs in positionally disordered systems in which there is no lattice. To illustrate this point, we examine the odd moduli of random materials built from point clouds. We take $N = 100$ Poisson distributed points in 2D and construct their Delaunay triangulation [Figs. 9(a) and 9(b)]. We assign to each edge a longitudinal bond stiffness $k \sim 1/a$, where a is the bond length—in contrast to our honeycomb and triangular lattices a now varies, and this protocol mimics a stiffness that arises from a material modulus and hence scales with overall spring length. Each plaquette is now activated with nonreciprocal torsion bonds of strength κ^a with a probability p. At each p we build 100 samples, generating a fresh triangulation and assignment of active plaquettes each time.

Examining the moduli of these random triangulations as a function of p [Fig. 9(c)] we again find a jump in K^o and a spike in μ as p crosses the site percolation threshold, in analogy to our results on periodic and random lattices (Fig. 2). We conclude that the basic phenomenology of the transition described in the main text is robust to the class of disorder considered—the key ingredients are a characteristic activity scale, and a sufficiently dilute material.

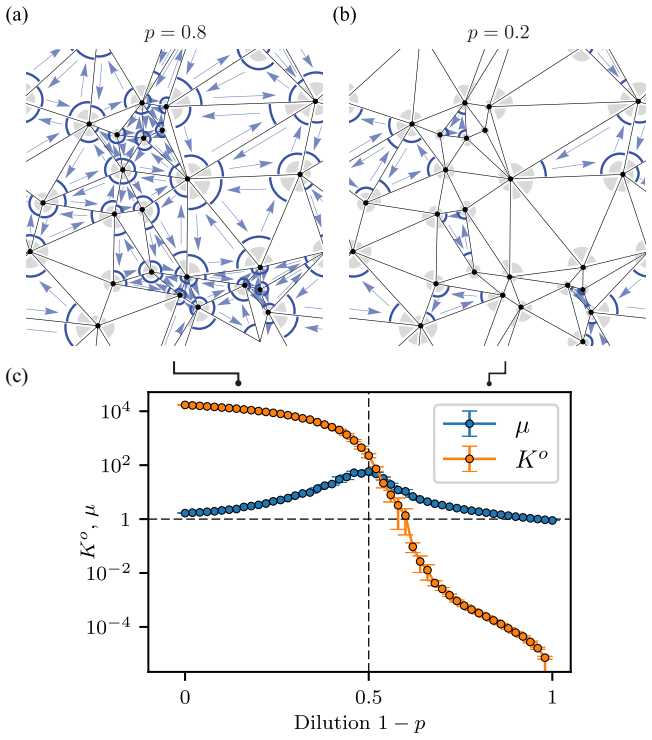


FIG. 9. Odd percolation in a disordered Delaunay triangulations. Just as in dilutions of honeycomb lattices, random triangulations of nonreciprocal torsional bonds also show a jump in the odd modulus K^o, and a spike in shear modulus μ, in the vicinity of the site percolation threshold $p = 1/2$. (a),(b) Two example Delaunay triangulations of randomly generated point clouds, with each triangle randomly assigned nonreciprocal torsional actuation of strength κ^a with probability p. Each bond has a longitudinal strength $k \sim 1/a$. (c) As the dilution crosses the site percolation threshold, the shear modulus μ spikes and the odd modulus K^o jumps, in analogy to Fig. 2 of the main text. The moduli are measured in units of $k\langle a\rangle^2$, where $\langle a\rangle$ is the average bond length. We fix $\kappa^a/k\langle a\rangle^2 = 100$ for all p.

APPENDIX H: QUANTIFYING FINITE SIZE EFFECTS IN OUR METAMATERIALS

Figure 1 shows that our periodic theory captures the key features of our metamaterials experiments: a decaying odd response, active stiffening, and plaquette locking, at high activity. These features are signatures of the percolation transition described in the main text. However there are some quantitative discrepancies: our theory overestimates K^o, μ and the plaquette shears S_1 and S_2 relative to experiment. One potential source of systematic bias is finite size effects: The experiments shown in Fig. 1 are performed on a 9×5 lattice of honeycombs, comprising $O(10)$ unit cells of the shown lattice (Sec. X), whereas our theory assumes a periodic lattice. To quantify finite size effects we develop ball-spring simulations of our lattices, in which we explicitly simulate our experimental protocol of applying a horizontal shear, and measuring the forces on the boundary nodes (Figs. 10 and 11).

We simulate the overdamped dynamics of a ball-spring mesh, where the forces on each node mimic our experiments. Each linkage exerts passive torques on the nodes with a torsional stiffness κ, and within an active plaquette nonreciprocal torques are additionally exerted as in Fig. 5. Longitudinal bonds are implemented with a finite but large spring stiffness k. We implement our boundary conditions with strain control: each node on the top and bottom of the lattice is constrained by a stiff spring, representing the rigid bar in our experiments. These constraining springs are horizontally displaced to mimic bar displacement [Fig. 10(a)]. Our simulation protocol mimics our experiments: we ramp through applied strains ϵ, and track boundary nodal forces [Figs. 10(b) and 10(c)] and internal shear modes [Figs. 10(d) and 10(e)]. At a given strain ϵ we test for internal convergence of net forces before moving to the next strain. Our simulations are performed using $\kappa = 1$, $k = 100$, and $k = 500$ for the constraining boundary springs. We use a forward Euler dynamics, where the frictional coefficient and timestep are interchangeable; we use timestep $dt = 10^{-3}$.

We first verify that we recover the odd modulus K^o, shear modulus μ and internal deformation fields S_1 and S_2 that are predicted by our periodic theory in a finite sample, provided that the system size is large [Figs. 10(f)–10(h)]. However, these simulations indeed indicate that there are finite size effects which can cause our simulated measurements to quantitatively deviate from the predictions of the periodic theory, while retaining the qualitative trends the theory predicts.

With this verification in hand, we now simulate lattices of the same dimensions as our experimental setup (Fig. 11), using the same protocol for generating and analyzing data that we use in our experiments (Sec. X, Figs. 12). As in our experiments, we apply large strains [$\epsilon \sim 0.1$], at which the stress-strain relations [Figs. 11(b) and 11(c)] and the relations between applied strain and internal shear modes [Figs. 11(d) and 11(e)] both become nonlinear. Linear elastic moduli and susceptibilities are extracted using the tangent modulus, by fitting a quadratic and taking the linear coefficient.

We find that our finite-size simulations push μ, S_1 and S_2 towards our experimental results, while leaving K^o within experimental error bars (Fig. 1). In particular, the systematic bias in μ [Fig. 11(g)] and S_1 [Fig. 11(h)], which exist even at $\kappa^a = 0$, are well accounted for by our finite size simulations. We conclude that the quantitative details of the relations S_1, S_2, K^o, and μ against κ^a/κ are indeed sensitive to finite size scaling and the imperfections of our experimental realization, yet the qualitative form of these relations is robust to these details.

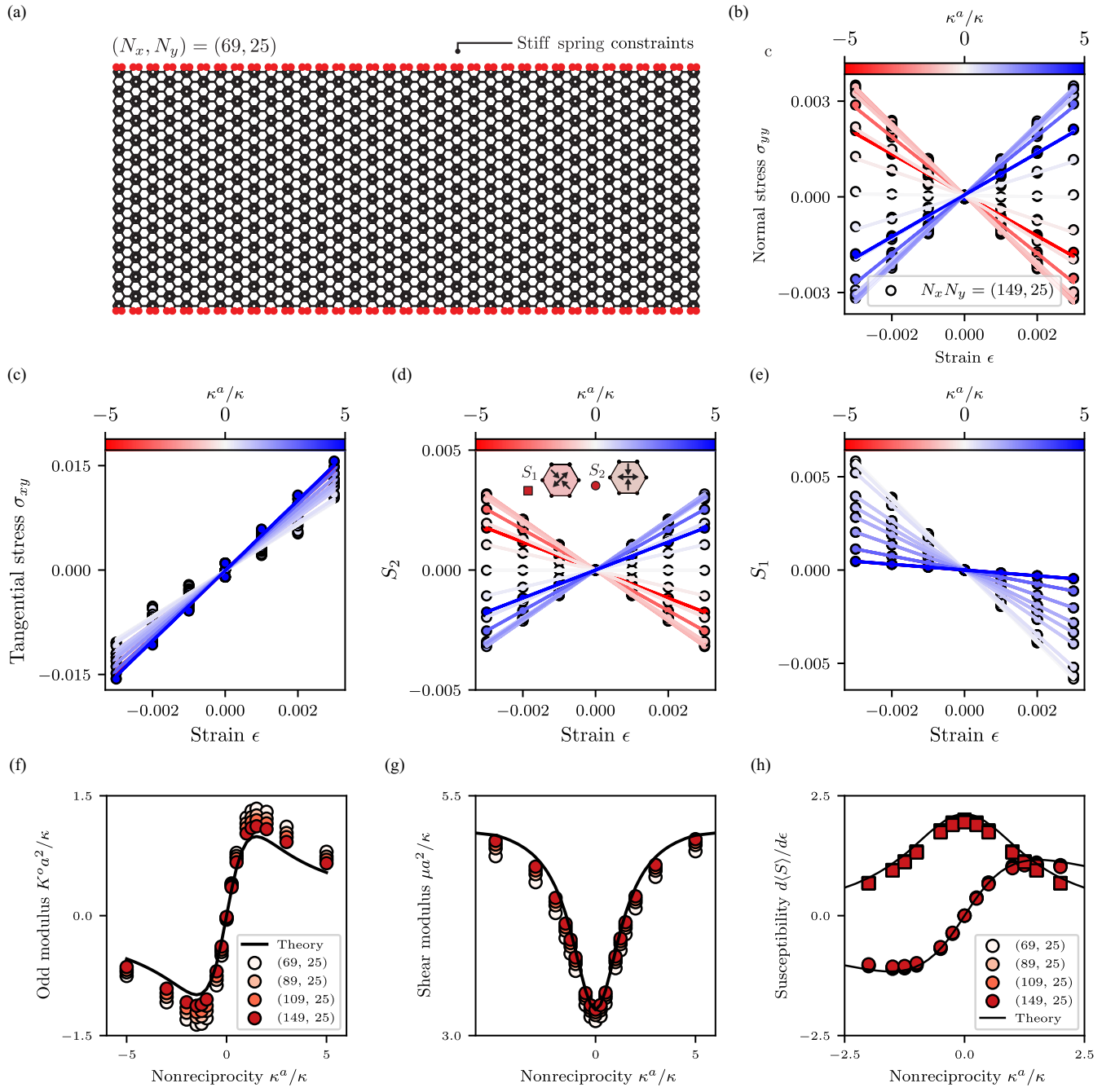


FIG. 10. Recovering our periodic theory in a large but finite lattice. (a) An example ball-spring lattice, composed of an $(N_x, N_y) = (69, 25)$ grid of honeycombs, with active plaquettes shown as hollow circles, and constraint points indicated in red. (b)–(e) We mimic our experimental protocol of horizontally shearing the lattice and measuring normal and tangential forces on constraint nodes, alongside averaged internal shear modes. For small applied strain ϵ, these relations are all linear. (f)–(h) We recover our theoretical predictions for K^o, μ, and $d\langle S\rangle/d\epsilon$ as a function of activity κ^a for large lattices.

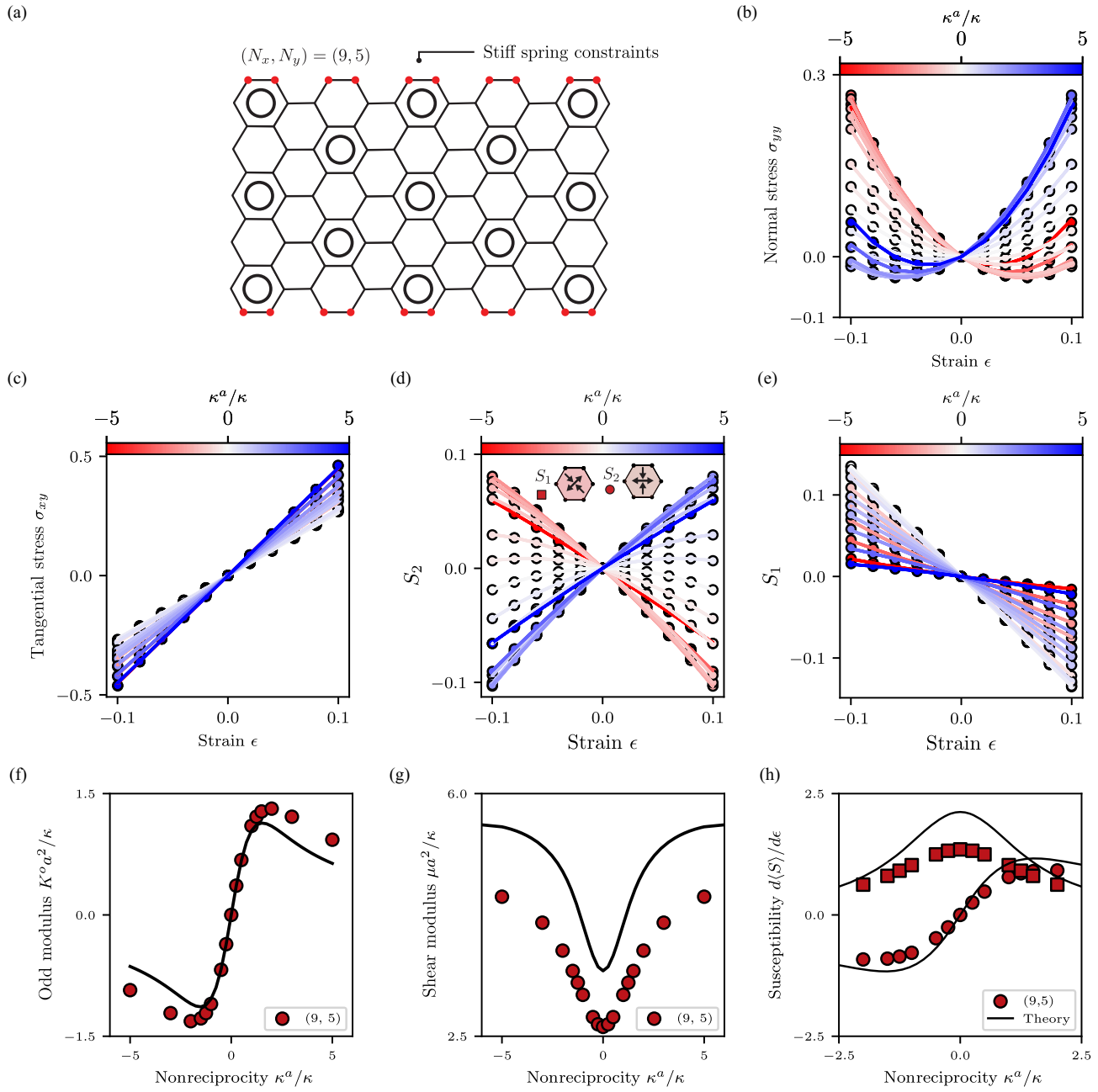


FIG. 11. Finite size effects in a numerical mimic of our experimental lattice. (a) A simulated $(N_x, N_y) = (9, 5)$ lattice mimicking our experiments. (b)–(e) We apply large strains $\epsilon \sim 0.1$ to mirror our experimental protocol, and track boundary forces and internal shear modes. At larger strains these relations become nonlinear—we extract tangent moduli and susceptibilities by fitting a quadratic and taking the linear coefficient. (f)–(h) For the (9, 5) lattice we see finite size corrections which slightly increase K^o at high activity and shift μ downwards for all activities. Correspondingly, $S_1 \sim \epsilon$ is downwards shifted for all κ^a, and S_2 is slightly off at high activities.

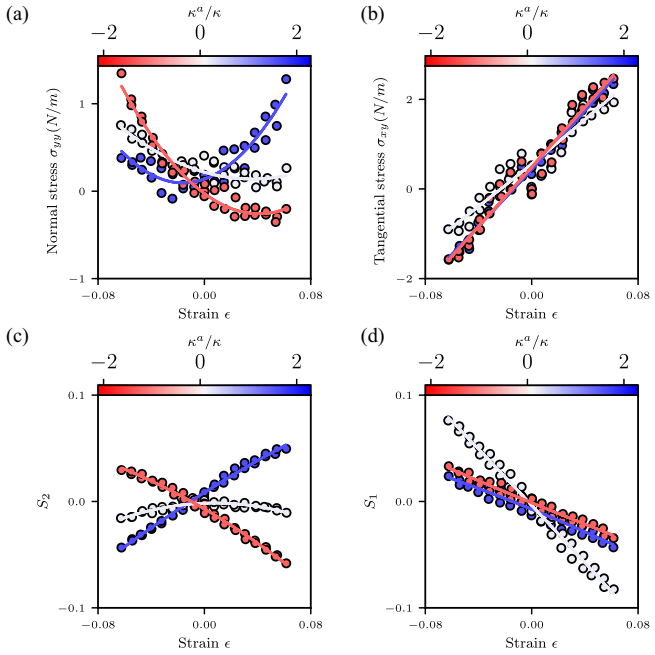


FIG. 12. Experimental data processing pipeline. (a),(b) Example data showing normal and tangential stresses σ_{yy}, σ_{xy} vs applied strain ϵ, corresponding to Fig. 1. We show traces at $\kappa^a/\kappa = 0, \pm 0.8$. The fits shown are quadratic. The slopes at the origin of these fits, $d\sigma_{yy}/d\epsilon$ and $d\sigma_{xy}/d\epsilon$, define K^o and μ. (c),(d) Average shear strains S_1 and S_2 across active plaquettes as a function of applied strain ϵ, with the slope of quadratic fits defining the susceptibility $d\langle S\rangle/d\epsilon$ of each shear mode.

APPENDIX I: CONSTRUCTION OF THE ROBOTIC MATERIALS

The metamaterial shown in Fig. 1(a) is composed of motorized vertices connected by plastic arms. Each vertex consists of a dc coreless motor (Motraxx CL1628) embedded in a cylindrical heatsink, an angular encoder (CUI AMT113S), and a microcontroller (ESP32) connected to a custom electronic board. The electronic board enables power conversion, interfacing between the sensor and motor, and communication between vertices. Each vertex has a diameter 50 mm, height 90 mm, and mass 0.2 kg. The power necessary to drive the motor is provided by an external 48V DC power source.

Rigid 3D-Printed arms connect each motor's drive shaft to the heat sink of the adjacent unit. The angle formed between the two arms at vertex i is denoted by θ_i. The on-board sensor measures θ_i at a sample rate of 100 Hz and communicates the measurement to nearest neighbors. In response to the incoming signal, vertex i exerts an active torsional force τ_i^a

$$\tau_i^a = \kappa^a(\delta\theta_{i+1} - \delta\theta_{i-1}), \tag{I1}$$

where $\delta\theta_i = \theta_i - \theta^0$ and θ^0 is the rest angle. The active stiffness κ^a was programmed by the microcontroller and calibrated by measuring torque-displacement slopes for different values of the electronic feedback. The coreless motor saturates at a maximum torque of $\tau_{\max} = 12$ mN m. Each link has a length of $a = 7.5$ cm. Adjacent vertices are also connected by a rubber band [blue in Fig. 1(a)] with a thickness 4 mm which provides a passive elastic torsional stiffness of $\kappa = 48$ mN m/rad. For further details see Ref. [16].

APPENDIX J: EXPERIMENTAL PROTOCOL

All experiments take place on top of a custom-made low-friction air table as the motors we use do not have enough torque to lift the weight of the unit cells. The table consists of two 1.5 m × 1.5 m plexiglass plates that sandwich 5 mm-wide air channels. The top plate is pierced by an array of holes (pitch 10 mm, diameter 1 mm) conveying air pressurised at 10 bars. Each motorized vertex floats on a thin layer of pressurized air without making contact with the table. The experiments are filmed via a Nikon D5600 camera equipped with a 50 mm lens, recording 2 Mpx images at 30 frames per second. A marker is placed on the top of each vertex, and we use the python package OpenCV to detect and track the position of each vertex with a spatial resolution of 0.8 mm.

In Fig. 1 of the main text, the top and bottom rows of hexagons in the lattice are constrained by 3D-printed fixtures attached to their top (bottom) vertices. These fixtures are in turn attached to rigid horizontal bars attached to a translation stage. Embedded in the horizontal bars are force sensors recording the normal force at a sample rate of 80 Hz and a precision of $\pm 0.2N$, allowing us to simultaneously apply a simple transverse shear and measure net forces on the bar. The metamaterial is then sheared to a maximum strain of 0.1 and allowed to equilibrate during 2 sec at intervals of 0.01 strain, after which shear and stress data are recorded.

To generate the plots shown in Fig. 1 we start with our recorded timeseries of vertex positions within the honeycomb lattice, combined with a time series of force and displacement data for the horizontal bar during a compression cycle. These data allow us to calculate the imposed macroscopic strain ϵ, the measured normal stress σ_{yy} and tangential stress σ_{xy} and the internal shear state $S_1 - S_2$ of every hexagon. Examples of these raw data are shown in Fig. 12.

To extract the odd and shear moduli shown in Figs. 1(c) and 1(d), we take the stress-strain curves given by the bar data and extract the slope at the origin. These curves are nonlinear at large strain, and to extract tangent moduli we fit a second order polynomial and take the slope at $\epsilon = 0$. To extract S_1 and S_2, we calculate

$$S_1 = \frac{1}{\sqrt{2}}(\delta\theta_1 - \delta\theta_3), \tag{J1}$$

$$S_2 = \frac{1}{\sqrt{6}}(\delta\theta_1 + \delta\theta_3 - 2\delta\theta_5), \tag{J2}$$

given in terms of the six angular deviations $\delta\theta_i$, $i = 1\ldots6$ within each hexagon from our tracking data. Schematics of each of these modes of deformation are shown in Fig. 1(b) of the main text. We take the amplitudes of these two shear modes, averaged across every active hexagonal plaquette in the lattice, to generate a series of S_1–S_2 data against applied strain ϵ for a given compression experiment. This data are shown in Figs. 12(c) and 12(d). Now, exactly as in the measurement of the odd modulus, we extract the slope of this strain curve against the imposed macroscopic strain ϵ. This slope $d\langle S\rangle/d\epsilon$ defines the susceptibility, which we plot as a function of activity in Figs. 1(g) and 1(h) of the main text. This procedure is also used on our simulation data Figs. 10, 11.

There are two differences between our experiments and simulations. First, the force sensors on each side of the lattice record different force signals due to substrate and solid friction. The data shown in Figs. 1(c) and 1(d) take their average and the error bars show the spread between sensors. Second, our experimentally constructed metamaterial has a bias towards a nonzero odd modulus even at zero activity [Fig. 12(a)]. We do not attribute this bias purely to finite size effects, because it is not present in our simulations Fig. 11. Instead, it is likely caused by an intrinsic chirality in the purely passive construction of our metamaterial. We measure odd moduli relative to this slight baseline bias. The experimental hinge length a, passive stiffness κ, and bar length are all taken from independently calibrated data as described in Sec. IX.

[1] M. C. Marchetti, J. F. Joanny, S. Ramaswamy, T. B. Liverpool, J. Prost, M. Rao, and R. A. Simha, *Hydrodynamics of soft active matter*, Rev. Mod. Phys. **85**, 1143 (2013).

[2] G. Gompper *et al.*, *The 2025 motile active matter roadmap*, J. Phys. Condens. Matter **37**, 143501 (2025).

[3] M. E. Cates and J. Tailleur, *Motility-Induced phase separation*, Annu. Rev. Condens. Matter Phys. **6**, 219 (2015).

[4] P. Bruno, *Impossibility of spontaneously rotating time crystals: A no-go theorem*, Phys. Rev. Lett. **111**, 070402 (2013).

[5] H. Watanabe and M. Oshikawa, *Absence of quantum time crystals*, Phys. Rev. Lett. **114**, 251603 (2015).

[6] M. Fruchart, R. Hanai, P. B. Littlewood, and V. Vitelli, *Non-reciprocal phase transitions*, Nature (London) **592**, 363 (2021).

[7] T. Liu, J.-Y. Ou, K. F. MacDonald, and N. I. Zheludev, *Photonic metamaterial analogue of a continuous time crystal*, Nat. Phys. **19**, 986 (2023).

[8] G. Volpe *et al.*, *Roadmap for animate matter*, J. Phys. Condens. Matter **37**, 333501 (2025).

[9] T. H. Tan, A. Mietke, J. Li, Y. Chen, H. Higinbotham, P. J. Foster, S. Gokhale, J. Dunkel, and N. Fakhri, *Odd dynamics of living chiral crystals*, Nature (London) **607**, 287 (2022).

[10] P. Baconnier, D. Shohat, C. H. López, C. Coulais, V. Démery, G. Düring, and O. Dauchot, *Selective and collective actuation in active solids*, Nat. Phys. **18**, 1234 (2022).

[11] Y. Zhang and É. Fodor, *Pulsating active matter*, Phys. Rev. Lett. **131**, 238302 (2023).

[12] H. Xu, Y. Huang, R. Zhang, and Y. Wu, *Autonomous waves and global motion modes in living active solids*, Nat. Phys. **19**, 46 (2023).

[13] S. Armon, M. S. Bull, A. Moriel, H. Aharoni, and M. Prakash, *Modeling epithelial tissues as active-elastic sheets reproduce contraction pulses and predict rip resistance*, Commun. Phys. **4**, 1 (2021).

[14] F. Pérez-Verdugo, S. Banks, and S. Banerjee, *Excitable dynamics driven by mechanical feedback in biological tissues*, Commun. Phys. **7**, 1 (2024).

[15] R. Alert, J. Casademunt, and J.-F. Joanny, *Active turbulence*, Annu. Rev. Condens. Matter Phys. **13**, 143 (2022).

[16] J. Veenstra, C. Scheibner, M. Brandenbourger, J. Binysh, A. Souslov, V. Vitelli, and C. Coulais, *Adaptive locomotion of active solids*, Nature (London) **639**, 935 (2025).

[17] B. Saintyves, M. Spenko, and H. M. Jaeger, *A self-organizing robotic aggregate using solid and liquid-like collective states*, Sci. Rob. **9**, eadh4130 (2024).

[18] M. R. Devlin, S. Kim, O. Campàs, and E. W. Hawkes, *Material-like robotic collectives with spatiotemporal control of strength and shape*, Science **387**, 880 (2025).

[19] R. Hanai, *Nonreciprocal frustration: Time crystalline order-by-disorder phenomenon and a spin-glass-like state*, Phys. Rev. X **14**, 011029 (2024).

[20] Y. Avni, M. Fruchart, D. Martin, D. Seara, and V. Vitelli, *Dynamical phase transitions in the nonreciprocal Ising model*, Phys. Rev. E **111**, 034124 (2025).

[21] Sarah A. M. Loos, Sabine H. L. Klapp, and T. Martynec, *Long-range order and directional defect propagation in the nonreciprocal XY model with vision cone interactions*, Phys. Rev. Lett. **130**, 198301 (2023).

[22] V. Raskatla, T. Liu, J. Li, K. F. MacDonald, and N. I. Zheludev, *Continuous space-time crystal state driven by nonreciprocal optical forces*, Phys. Rev. Lett. **133**, 136202 (2024).

[23] V. Liška, T. Zemánková, P. Jákl, M. Šiler, S. H. Simpson, P. Zemánek, and O. Brzobohatý, *PT-like phase transition and limit cycle oscillations in non-reciprocally coupled optomechanical oscillators levitated in vacuum*, Nat. Phys. **20**, 1622 (2024).

[24] M. Reisenbauer, H. Rudolph, L. Egyed, K. Hornberger, A. V. Zasedatelev, M. Abuzarli, B. A. Stickler, and U. Delić, *Non-Hermitian dynamics and non-reciprocity of optically coupled nanoparticles*, Nat. Phys. **20**, 1629 (2024).

[25] F. Ruesink, M.-A. Miri, A. Alù, and E. Verhagen, *Nonreciprocity and magnetic-free isolation based on optomechanical interactions*, Nat. Commun. **7**, 13662 (2016).

[26] S. Weidemann, M. Kremer, T. Helbig, T. Hofmann, A. Stegmaier, M. Greiter, R. Thomale, and A. Szameit, *Topological funneling of light*, Science **368**, 311 (2020).

[27] R. Fleury, D. L. Sounas, C. F. Sieck, M. R. Haberman, and A. Alù, *Sound isolation and giant linear nonreciprocity in a compact acoustic circulator*, Science **343**, 516 (2014).
[28] M. X. Lim, B. VanSaders, and H. M. Jaeger, *Acoustic manipulation of multi-body structures and dynamics*, Rep. Prog. Phys. **87**, 064601 (2024).
[29] T. Beatus, T. Tlusty, and R. Bar-Ziv, *Phonons in a one-dimensional microfluidic crystal*, Nat. Phys. **2**, 743 (2006).
[30] E. S. Bililign, F. Balboa Usabiaga, Y. A. Ganan, A. Poncet, V. Soni, S. Magkiriadou, M. J. Shelley, D. Bartolo, and W. T. M. Irvine, *Motile dislocations knead odd crystals into whorls*, Nat. Phys. **18**, 212 (2022).
[31] F. Gu, B. Guiselin, N. Bain, I. Zuriguel, and D. Bartolo, *Emergence of collective oscillations in massive human crowds*, Nature (London) **638**, 112 (2025).
[32] Z. You, A. Baskaran, and M. C. Marchetti, *Nonreciprocity as a generic route to traveling states*, Proc. Natl. Acad. Sci. U.S.A. **117**, 19767 (2020).
[33] F. Brauns and M. C. Marchetti, *Nonreciprocal pattern formation of conserved fields*, Phys. Rev. X **14**, 021014 (2024).
[34] S. Saha, J. Agudo-Canalejo, and R. Golestanian, *Scalar active mixtures: The nonreciprocal Cahn-Hilliard model*, Phys. Rev. X **10**, 041009 (2020).
[35] A. Dinelli, J. O'Byrne, A. Curatolo, Y. Zhao, P. Sollich, and J. Tailleur, *Non-reciprocity across scales in active mixtures*, Nat. Commun. **14**, 7035 (2023).
[36] S. Osat and R. Golestanian, *Non-reciprocal multifarious self-organization*, Nat. Nanotechnol. **18**, 79 (2023).
[37] C. H. Meredith, P. G. Moerman, J. Groenewold, Y.-J. Chiu, W. K. Kegel, A. van Blaaderen, and L. D. Zarzar, *Predator-prey interactions between droplets driven by non-reciprocal oil exchange*, Nat. Chem. **12**, 1136 (2020).
[38] C. Scheibner, A. Souslov, D. Banerjee, P. Surówka, W. T. M. Irvine, and V. Vitelli, *Odd elasticity*, Nat. Phys. **16**, 475 (2020).
[39] M. Fruchart, C. Scheibner, and V. Vitelli, *Odd viscosity and odd elasticity*, Annu. Rev. Condens. Matter Phys. **14**, 471 (2023).
[40] C. P. Goodrich, A. J. Liu, and S. R. Nagel, *The principle of independent bond-level response: Tuning by pruning to exploit disorder for global behavior*, Phys. Rev. Lett. **114**, 225501 (2015).
[41] J. W. Rocks, N. Pashine, I. Bischofberger, C. P. Goodrich, A. J. Liu, and S. R. Nagel, *Designing allostery-inspired response in mechanical networks*, Proc. Natl. Acad. Sci. U.S.A. **114**, 2520 (2017).
[42] L. Yan, R. Ravasio, C. Brito, and M. Wyart, *Architecture and coevolution of allosteric materials*, Proc. Natl. Acad. Sci. U.S.A. **114**, 2526 (2017).
[43] M. Stern, D. Hexner, J. W. Rocks, and A. J. Liu, *Supervised learning in physical networks: From machine learning to learning machines*, Phys. Rev. X **11**, 021045 (2021).
[44] Y. Du, J. Veenstra, R. van Mastrigt, and C. Coulais, *Metamaterials that learn to change shape*, arXiv:2501.11958.
[45] P. Ronceray, C. P. Broedersz, and M. Lenz, *Stress-dependent amplification of active forces in nonlinear elastic media*, Soft Matter **15**, 331 (2019).
[46] J. Duque, A. Bonfanti, J. Fouchard, L. Baldauf, S. R. Azenha, E. Ferber, A. Harris, E. H. Barriga, A. J. Kabla, and G. Charras, *Rupture strength of living cell monolayers*, Nat. Mater. **23**, 1563 (2024).
[47] Y.-C. Chao, S. Gokhale, L. Lin, A. Hastewell, A. Bacanu, Y. Chen, J. Li, J. Liu, H. Lee, J. Dunkel, and N. Fakhri, *Selective excitation of work-generating cycles in non-reciprocal living solids*, Nat. Phys. (2026).
[48] See Supplemental Material at http://link.aps.org/supplemental/10.1103/flhb-kjyd for Supplementary movies S1 and S2, which show experimental data and analysis corresponding to Fig. 1, and deformations of the ball-spring models shown in Fig. 2.
[49] S. H. Choi, Z.-F. Huang, and N. Goldenfeld, *Noise-driven odd elastic waves in living chiral active matter*, arXiv:2411.09615.
[50] C. Scheibner, William T. M. Irvine, and V. Vitelli, *Non-Hermitian band topology and skin modes in active elastic media*, Phys. Rev. Lett. **125**, 118001 (2020).
[51] M. van Hecke, *Jamming of soft particles: Geometry, mechanics, scaling and isostaticity*, J. Phys. Condens. Matter **22**, 033101 (2009).
[52] F. Burla, J. Tauber, S. Dussi, J. van der Gucht, and G. H. Koenderink, *Stress management in composite biopolymer networks*, Nat. Phys. **15**, 549 (2019).
[53] J. Veenstra, O. Gamayun, X. Guo, A. Sarvi, C. V. Meinersen, and C. Coulais, *Non-reciprocal topological solitons in active metamaterials*, Nature (London) **627**, 528 (2024).
[54] R. Mandal, R. Huang, M. Fruchart, P. G. Moerman, S. Vaikuntanathan, A. Murugan, and V. Vitelli, *Learning dynamical behaviors in physical systems*, arXiv:2406.07856.
[55] J. Alvarado, M. Sheinman, A. Sharma, F. C. MacKintosh, and G. H. Koenderink, *Molecular motors robustly drive active gels to a critically connected state*, Nat. Phys. **9**, 591 (2013).
[56] T. Wyse Jackson, J. Michel, P. Lwin, L. A. Fortier, M. Das, L. J. Bonassar, and I. Cohen, *Structural origins of cartilage shear mechanics*, Sci. Adv. **8**, eabk2805 (2022).
[57] S. Chen, D. E. Gökmen, M. Fruchart, M. Krumbein, P. Silberzan, V. Yashunsky, and V. Vitelli, *Chirality across scales in tissue dynamics*, arXiv:2506.12276.
[58] N. I. Petridou, B. Corominas-Murtra, C.-P. Heisenberg, and E. Hannezo, *Rigidity percolation uncovers a structural basis for embryonic tissue phase transitions*, Cell **184**, 1914 (2021).
[59] C. Jorge, A. Chardac, A. Poncet, and D. Bartolo, *Active hydraulics laws from frustration principles*, Nat. Phys. **20**, 303 (2024).
[60] Z. G. Nicolaou and A. E. Motter, *Mechanical metamaterials with negative compressibility transitions*, Nat. Mater. **11**, 608 (2012).
[61] P. Ducarme, B. Weber, M. van Hecke, and J. T. B. Overvelde, *Exotic mechanical properties enabled by countersnapping instabilities*, Proc. Natl. Acad. Sci. U.S.A. **122**, e2423301122 (2025).
[62] T. C. Lubensky, C. L. Kane, X. Mao, A. Souslov, and K. Sun, *Phonons and elasticity in critically coordinated lattices*, Rep. Prog. Phys. **78**, 073901 (2015).
[63] Zenodo repository: 10.5281/zenodo.18775584.